



<b>Publication Year</b>	2021
<b>Acceptance in OA</b>	2022-03-16T15:56:11Z
<b>Title</b>	The GAPS Programme at TNG. XXXI. The WASP-33 system revisited with HARPS-N
<b>Authors</b>	BORSA, Francesco, LANZA, Antonino Francesco, Raspantini, I., RAINER, Monica, Fossati, L., Brogi, M., Di Mauro, M. P., GRATTON, Raffaele, PINO, Lorenzo, BENATTI, SERENA, BIGNAMINI, ANDREA, BONOMO, ALDO STEFANO, CLAUDI, Riccardo, Esposito, M., FRUSTAGLI, GIUSEPPE, MAGGIO, Antonio, MALDONADO PRADO, Jesus, Mancini, L., MICELA, Giuseppina, NASCIMBENI, VALERIO, PORETTI, Ennio, SCANDARIATO, GAETANO, SICILIA, Daniela, SOZZETTI, Alessandro, Boschin, W., COSENTINO, Rosario, COVINO, Elvira, DESIDERA, Silvano, Di Fabrizio, L., Fiorenzano, A. F. M., Harutyunyan, A., KNAPIC, Cristina, MOLINARI, Emilio Carlo, PAGANO, Isabella, Pedani, M., Piotto, G.
<b>Publisher's version (DOI)</b>	10.1051/0004-6361/202140559
<b>Handle</b>	<a href="http://hdl.handle.net/20.500.12386/31627">http://hdl.handle.net/20.500.12386/31627</a>
<b>Journal</b>	ASTRONOMY & ASTROPHYSICS
<b>Volume</b>	653

# The GAPS Programme at TNG

## XXXI. The WASP-33 system revisited with HARPS-N<sup>★</sup>

F. Borsa<sup>1</sup>, A. F. Lanza<sup>2</sup>, I. Raspantini<sup>3</sup>, M. Rainer<sup>4</sup>, L. Fossati<sup>5</sup>, M. Brogi<sup>6,7,8</sup>, M. P. Di Mauro<sup>9</sup>, R. Gratton<sup>10</sup>, L. Pino<sup>4</sup>, S. Benatti<sup>11</sup>, A. Bignamini<sup>12</sup>, A. S. Bonomo<sup>7</sup>, R. Claudi<sup>10</sup>, M. Esposito<sup>13</sup>, G. Frustagli<sup>3,1</sup>, A. Maggio<sup>11</sup>, J. Maldonado<sup>11</sup>, L. Mancini<sup>14,15,7</sup>, G. Micela<sup>11</sup>, V. Nascimbeni<sup>10</sup>, E. Poretti<sup>1,16</sup>, G. Scandariato<sup>2</sup>, D. Sicilia<sup>2</sup>, A. Sozzetti<sup>7</sup>, W. Boschin<sup>16,17,18</sup>, R. Cosentino<sup>16</sup>, E. Covino<sup>19</sup>, S. Desidera<sup>10</sup>, L. Di Fabrizio<sup>16</sup>, A. F. M. Fiorenzano<sup>16</sup>, A. Harutyunyan<sup>16</sup>, C. Knapic<sup>12</sup>, E. Molinari<sup>20</sup>, I. Pagano<sup>2</sup>, M. Pedani<sup>16</sup>, and G. Piotto<sup>21</sup>

(Affiliations can be found after the references)

Received 14 February 2021 / Accepted 21 May 2021

### ABSTRACT

**Context.** Giant planets in short-period orbits around bright stars represent optimal candidates for atmospheric and dynamical studies of exoplanetary systems.

**Aims.** We aim to analyse four transits of WASP-33b observed with the optical high-resolution HARPS-N spectrograph to confirm its nodal precession, study its atmosphere, and investigate the presence of star-planet interactions.

**Methods.** We extracted the mean line profiles of the spectra using the least-squares deconvolution method, and we analysed the Doppler shadow and the radial velocities. We also derived the transmission spectrum of the planet, correcting it for the stellar contamination due to rotation, centre-to-limb variations, and pulsations.

**Results.** We confirm the previously discovered nodal precession of WASP-33b, almost doubling the time coverage of the inclination and projected spin-orbit angle variation. We find that the projected obliquity reached a minimum in 2011, and we used this constraint to derive the geometry of the system, and in particular its obliquity at that epoch ( $\epsilon = 113.99^\circ \pm 0.22^\circ$ ) and the inclination of the stellar spin axis ( $i_s = 90.11^\circ \pm 0.12^\circ$ ). We also derived the gravitational quadrupole moment of the star  $J_2 = (6.73 \pm 0.22) \times 10^{-5}$ , which we find to be in close agreement with the theoretically predicted value. Small systematics errors are computed by shifting the date of the minimum projected obliquity. We present detections of H $\alpha$  and H $\beta$  absorption in the atmosphere of the planet, with a contrast almost twice as small as that previously detected in the literature. We also find evidence for the presence of a pre-transit signal, which repeats in all four analysed transits and should thus be related to the planet. The most likely explanation lies in a possible excitation of a stellar pulsation mode by the presence of the planetary companion.

**Conclusions.** A future common analysis of all available datasets in the literature will help shed light on the possibility that the observed Balmer lines' transit depth variations are related to stellar activity and pulsation, and to set constraints on the planetary temperature–pressure structure and thus on the energetics possibly driving atmospheric escape. A complete orbital phase coverage of WASP-33b with high-resolution spectroscopic (and spectro-polarimetric) observations could help us to understand the nature of the pre-transit signal.

**Key words.** techniques: spectroscopic – planetary systems – planets and satellites: atmospheres – stars: individual: WASP-33 – techniques: radial velocities

## 1. Introduction

Transiting exoplanets orbiting intermediate-mass (e.g. A-type) stars on short-period ( $P_{\text{orb}} \leq 5$  days) orbits are excellent laboratories for atmospheric and dynamical studies. The high day-side equilibrium temperatures of these ultra-hot Jupiters (UHJs,  $T_{\text{eq}} \geq 2200$  K) cause the thermal dissociation of most molecules (e.g. Lothringer et al. 2018; Arcangeli et al. 2018). Depending on the heat transfer efficiency in the atmosphere, there might also be variations in the chemical composition of the day-side, night-side and terminator of the planet (e.g., Parmentier et al. 2018). Orbiting at short distances from their parent star, the strong stellar ultraviolet irradiation makes the

planetary atmosphere undergo a significant mass loss, affecting its composition and evolution (e.g. Fossati et al. 2018a).

Short-period systems are also interesting because they experience strong tidal interactions between the planet and its host star. Star-planet tidal interactions could modify the stellar rotation rate along the system's evolution (Gallet et al. 2018), cause planet oblateness (Akinkanmi et al. 2019), suppress stellar activity (Fossati et al. 2018b), and induce stellar pulsations (de Wit et al. 2017). The measure of the projected spin-orbit angle either with radial velocities (RVs) through the Rossiter-McLaughlin effect (RM, Rossiter 1924; McLaughlin 1924), or with the Doppler tomography technique (e.g. Collier Cameron et al. 2010a) can help to shed light on a system evolution history (e.g. Fabrycky & Winn 2009).

In this context, WASP-33b (Collier Cameron et al. 2010b) is a very intriguing target. It is a UHJ ( $M_p \sim 2.2 M_{\text{Jup}}$ ,  $R_p \sim 1.6 R_{\text{Jup}}$ ) orbiting in  $\sim 1.21$  days a bright  $\delta$ -Scuti A-type star ( $V = 8.3$ ,  $T_{\text{eff}} \sim 7500$  K,  $v \sin i_s \sim 86$  km s<sup>-1</sup>) with a highly misaligned

<sup>★</sup> Based on observations made with the Italian Telescopio Nazionale Galileo (TNG) operated on the island of La Palma by the Fundacion Galileo Galilei of the INAF at the Spanish Observatorio Roque de los Muchachos of the IAC in the frame of the program Global Architecture of the Planetary Systems (GAPS).

projected spin–orbit angle:  $\lambda \sim -110$  degrees (Collier Cameron et al. 2010b; Lehmann et al. 2015). Stellar non-radial pulsations were already noted spectroscopically in the discovery paper (Collier Cameron et al. 2010b). Photometric oscillations of the star were first reported by Herrero et al. (2011), and the stellar pulsation spectrum has been analysed in different studies (Kovács et al. 2013; von Essen et al. 2014; Mkrtrichian 2015; von Essen et al. 2020). Because of its easily detected stellar pulsations, the WASP-33 system has been considered a good candidate for the detection of star-planet interactions (Herrero et al. 2011). WASP-33b was also noted as a possible target for which both classical and relativistic node precessional effects could be evidenced within a reasonable amount of time (Iorio 2011, 2016); indeed, classical node precessional effects were subsequently detected by Johnson et al. (2015) and Watanabe et al. (2020).

Its atmosphere has also been the subject of different studies. The probable presence of a temperature inversion in its atmosphere (Haynes et al. 2015; von Essen et al. 2015) was best explained by the presence of titanium oxide (TiO); however the detection of TiO using high-resolution spectroscopy is debated (Nugroho et al. 2017; Herman et al. 2020). Other results include the first indication of aluminum oxide (AlO) in an exoplanet using low-resolution spectrophotometry (von Essen et al. 2019), the detection of ionised calcium (Ca II H&K) up to very high upper-atmosphere layers close to the planetary Roche lobe (Yan et al. 2019), and the detection of Balmer lines (Yan et al. 2021; Cauley et al. 2021). The existence of a thermal inversion was recently confirmed with the detection of Fe I in emission using high-resolution observations (Nugroho et al. 2020).

Driven by the intriguing characteristics of the system, in this work we analysed new transits of WASP-33b taken with the HARPS-N high-resolution spectrograph, looking for confirmation of the nodal precession and exploring its atmosphere. This manuscript is organised as follows. We first present our data in Sect. 2, then analyse the planetary Doppler shadow and the in-transit RVs also studying the precession of the orbital plane and the spin of the host star (Sects. 3 and 4). We studied the planetary atmosphere focusing on H $\alpha$  and H $\beta$  absorption in Sect. 5, finding a pre-transit signal coherent with the planetary orbital period discussed in Sect. 6. Then, we looked for other atmospheric species with the cross-correlation technique described in Sect. 7. We end with our summary and conclusions in Sect. 8.

## 2. Data sample

We observed WASP-33 during four transits using the high-resolution (resolving power  $R \sim 115\,000$ ) HARPS-N spectrograph (Cosentino et al. 2012) mounted at the Telescopio Nazionale Galileo on La Palma island and covering the 380–690 nm wavelength range. The first two transits were observed with HARPS-N only (program A34TAC42, PI Nascimbeni), while the other two were taken in the framework of the GAPS project (Covino et al. 2013). The latter were observed using the GIARPS configuration (Claudi et al. 2017), but in this manuscript we focus only on the HARPS-N data.

The transit of WASP-33b lasts 2 h 48 min. Three transit observations were monitored with exposures of 600 s, while for one we used a longer cadence (900 s exposure). While fiber A of the spectrograph was centred on the target, for all the transits fiber B was simultaneously monitoring the sky to check for possible atmospheric emission contamination. The log of the observations is reported in Table 1.

The quality of transit two rapidly decreases after the transit ingress due to weather conditions, we thus decided to not include

**Table 1.** WASP-33 HARPS-N observations log.

Transit number	Night <sup>(1)</sup>	Exposure time	$N_{\text{obs}}$	$S/N_{\text{ave}}$
1	28 Sep. 2016	600 s	40	107
2 <sup>(*)</sup>	20 Oct. 2016	600 s	32	90
3	12 Jan. 2018	900 s	23	166
4	02 Jan. 2019	600 s	33	115

**Notes.** <sup>(\*)</sup>Weather conditions rapidly worsening. <sup>(1)</sup>Start of night civil date.

it in the analysis of the transmission spectrum, Doppler shadow, and RVs, but we do include it in Sect. 6, where we look at the pre-transit portion of the data.

## 3. Precession of the orbital plane and stellar spin axis

WASP-33 is a  $\delta$ -Sct A-type star. Since no default A-type mask is supported by the HARPS-N DRS pipeline (Cosentino et al. 2014), we followed the approach presented in Borsa et al. (2019) and extracted the mean line profiles using the least-squares deconvolution (LSD) software (Donati et al. 1997). This software performs a least-squares deconvolution of the normalised spectra with a theoretical line mask extracted from the Vienna Atomic Line Database (VALD, Piskunov et al. 1995). We used a stellar mask with  $T_{\text{eff}} = 7500$  K,  $\log g = 4.0$ , and solar metallicity. We accurately re-normalised the spectra (order-by-order by using polynomials; see Rainer et al. (2016) for a detailed description of the procedure) and converted them to the required format, working only on the wavelength regions 441.5–480.5 nm, 491.5–528.5 nm, 536.5–587.0 nm, 605.0–626.5 nm, and 633.5–645.0 nm, hence cutting the blue orders where the signal-to-noise ratio (S/N) was very low due to the instrument efficiency, the Balmer lines, and the regions where most of the telluric lines are found. We then created mean line profile residuals by dividing all the mean line profiles by a master out-of-transit mean line profile for each transit observed. As already evidenced by Collier Cameron et al. (2010b) and Johnson et al. (2015), the Doppler shadow of the planet is clearly visible as well as the stellar pulsations (Fig. 1, left panel). We note that the pulsations are more evident on the edge of the lines with respect to the centre, which is a hint of non-radial pulsations (see also Collier Cameron et al. 2010b).

For planets with projected spin-orbit angles close to  $90^\circ$ , nodal precession can be more easily detected during observations spanning several years (Watanabe et al. 2020). WASP-33b is one of the two reported cases where the exoplanet orbit has been found to show nodal precession (Johnson et al. 2015; Watanabe et al. 2020), with the other case being Kepler-13Ab (Szabó et al. 2012; Herman et al. 2018). Since our dataset extends the timespan of the reported orbital variations, we tried to see if this was also visible in our data. We removed stellar pulsations independently for each single transit using Fourier transform filtering (Fig. 1) following the method presented in Johnson et al. (2015). This exploits the fact that pulsations (prograde) and Doppler shadow (retrograde) propagate in opposite directions: their frequency components thus tend to be separated in the two-dimensional Fourier transform of the line profile residuals' time series (Johnson et al. 2015). We then performed a fit to the Doppler shadow. The Doppler shadow model is taken from EXOFASTv2 (Eastman 2017; Eastman et al. 2019), passed through the Fourier filter, and fitted to the data in a Bayesian

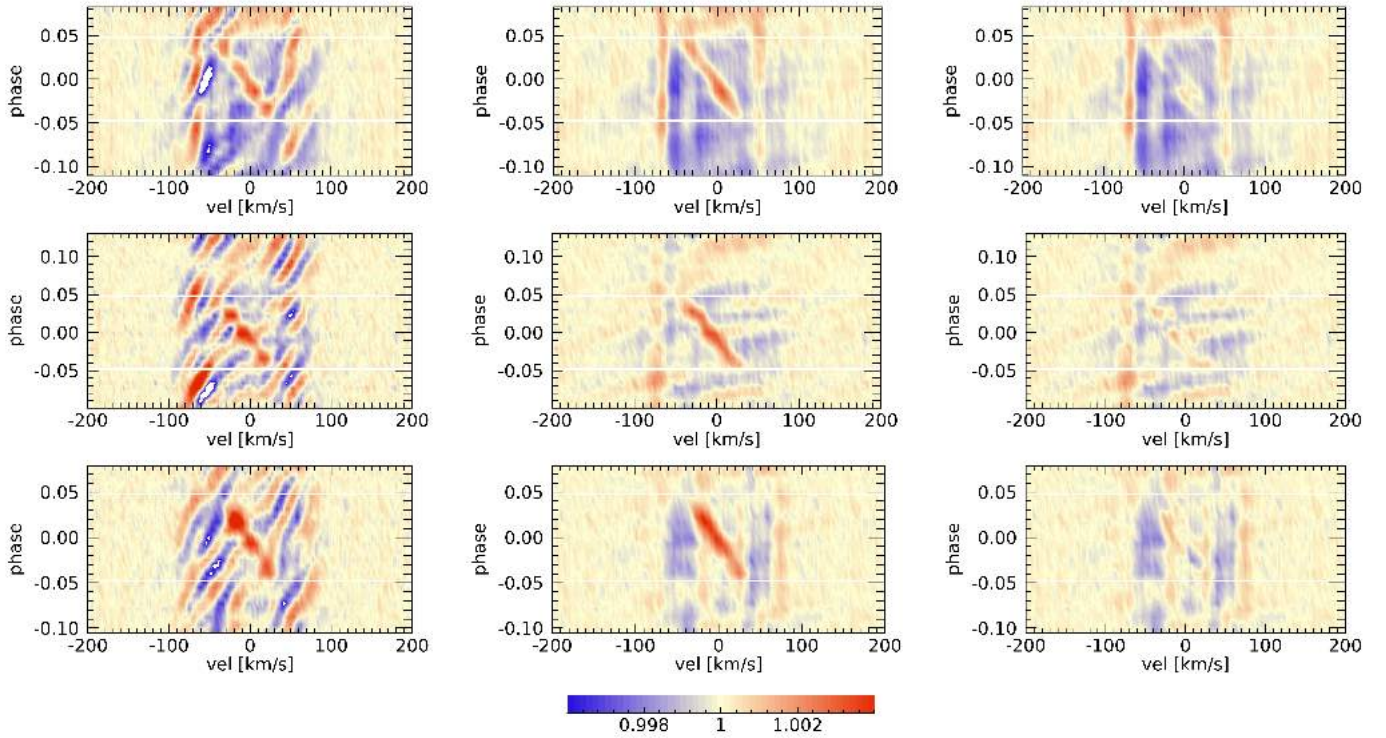


**Fig. 1.** Tomography of the pulsation filtering from the mean line profile residuals. *From top to bottom:* transits 1, 3, and 4, respectively. *Left panels:* contour plot of the mean line profile residuals. *Central panels:* same as for left panels, but after filtering in the Fourier space. *Right panels:* same as for central panels, after subtracting the best-fit Doppler shadow model. The horizontal white lines show the beginning and end of the transit.

framework by employing a differential evolution Markov chain Monte Carlo (DE-MCMC) technique (Ter Braak 2006; Eastman et al. 2013), running five DE-MCMC chains of 100,000 steps and discarding the burn-in. We fixed  $v \sin i_s$ ,  $a/R_s$ ,  $T_0$ , period,  $R_p/R_s$  to the values of Table 2. We left the projected spin-orbit angle  $\lambda$  and the inclination angle  $i$ , for which we set uninformative priors, as free parameters. The medians and the 15.86% and 84.14% quantiles of the posterior distributions were taken as the best values and  $1\sigma$  uncertainties.

Our results (Fig. 2, Table 2), together with the previous measurements of Watanabe et al. (2020), confirm the precession of the planetary orbit and that the obliquity projected on the plane of the sky  $\lambda$  reached a minimum in 2011. This allows us to determine the inclination of the stellar spin axis to the line of sight  $i_s$  and the obliquity  $\epsilon$  at the epoch when  $d\lambda/dt = 0$ , thus allowing a more precise description of the precession of the system and the measure of the stellar gravitational quadrupole moment  $J_2$ . We describe the method applied to determine the system geometry as well as the rate of precession of the nodes of the orbital plane in Appendix A.

The rate of change of the inclination angle of the orbital plane  $i$  can be regarded as constant over the time span of the observations ( $\sim 10$  yr) because it is much shorter than the precession period ( $\sim 1100$  yr; see below). It is measured by a weighted linear best fit to the data in Fig. 2 (upper panel), giving  $di/dt = 0.324 \pm 0.006 \text{ deg yr}^{-1}$ , while the epoch when  $d\lambda/dt = 0$  is assumed to coincide with the transit observed on 19 October 2011, when  $i = 87.56^\circ \pm 0.037^\circ$  and  $\lambda = -114.01^\circ \pm 0.22^\circ$  (Watanabe et al. 2020). Given the uncertainty on such an epoch, we report the systematic deviations in the derived model parameters corresponding to a shift of the epoch of  $d\lambda/dt = 0$  by  $\pm 500$  days since the assumed epoch, respectively (Table A.1). To

compute these deviations, we assume that  $di/dt$  has the same value as above, while we linearly interpolated for the parameter  $i$  and cubically interpolated for the parameter  $\lambda$  to find their values at the two epochs. For each parameter, we report the standard deviation as a measure of the statistical error, while in brackets we add the systematic deviation when  $d\lambda/dt = 0$  at the later epoch and the deviation when  $d\lambda/dt = 0$  at the earlier epoch, respectively. We note that the two deviations have the same sign when the parameter reached an extremum in between the considered epochs.

Following the method described in Appendix A, we find that the stellar spin is perpendicular to the line of sight ( $i_s = 90.11^\circ \pm 0.12^\circ$  ( $-0.026^\circ; -0.015^\circ$ )), while the obliquity  $\epsilon = 113.99^\circ \pm 0.22^\circ$  ( $-0.24^\circ; -0.67^\circ$ ) at the epoch of the transit on 19 October 2011. From the spectroscopic stellar  $v \sin i_s$ ,  $i_s$ , and stellar radius, we estimate a rotation period of the star of  $0.884 \pm 0.02$  days, not significantly affected by the systematic errors on  $i_s$  because it is close to  $90^\circ$ . The precession rate of the nodes of the orbital plane is found to be  $-0.325 \pm 0.006$  ( $6.7 \times 10^{-5}; 1.1 \times 10^{-4}$ )  $\text{deg yr}^{-1}$ , giving a precession period of  $1108 \pm 19$  (0.23; 0.38) yr, slightly longer than that determined by Johnson et al. (2015). The time interval during which transits by WASP-33b are observable is thus of  $\sim 97$  yr, centred around 2019, which is slightly longer than their interval of about  $\sim 88$  yr.

Our inclination  $i_s$  of the stellar spin axis to the line of sight is different from the value found by Iorio (2016) because his determination was based on the parameters derived only from the transits of 2008 and 2014 as reported by Johnson et al. (2015). This led Iorio to consider a constant precession rate of the angle  $I$  of his model, while our more extended dataset shows that  $dI/dt$  is variable and became zero around 2011. In Appendix A.5, we

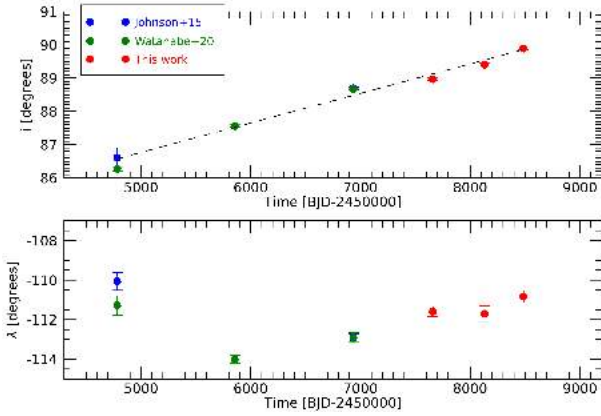


**Fig. 2.** Measurements of the inclination angle  $i$  (*top panel*) and of the projected spin-orbit angle  $\lambda$  (*bottom panel*) as a function of time. The dashed line shows the linear trend discussed in Sect. 3.

**Table 2.** Stellar and orbital parameters adopted in this work.

Parameter	Value	Reference
<b>WASP-33</b>		
<i>Stellar parameters</i>		
$T_{\text{eff}}$ (K)	$7430 \pm 100$	Yan et al. 2019
$\text{Log } g$	$4.3 \pm 0.2$	Yan et al. 2019
[Fe/H]	$-0.1 \pm 0.2$	Yan et al. 2019
$R_s$ ( $R_{\odot}$ )	$1.509 \pm 0.025$	Yan et al. 2019
$M_s$ ( $M_{\odot}$ )	$1.561 \pm 0.06$	Yan et al. 2019
$v \sin i_s$ ( $\text{km s}^{-1}$ )	$86.4 \pm 0.5$	This work
$P_{\text{rot}}$ (days)	$0.884 \pm 0.02$	This work
<i>Orbital parameters</i>		
Period (days)	1.219870897	Yan et al. 2019
$T_0$ (BJD-2 450 000)	4163.22449	Yan et al. 2019
$R_p/R_s$	0.11177	Yan et al. 2019
$a/R_s$	$3.69 \pm 0.05$	Yan et al. 2019
$e$	0.0	Assumed
$i$ (degrees)	$88.97 \pm 0.04$	This work, transit 1
$i$ (degrees)	$89.40 \pm 0.05$	This work, transit 3
$i$ (degrees)	$89.89 \pm 0.03$	This work, transit 4
$\lambda$ (degrees)	$-111.59 \pm 0.25$	This work, transit 1
$\lambda$ (degrees)	$-111.70 \pm 0.39$	This work, transit 3
$\lambda$ (degrees)	$-110.83 \pm 0.30$	This work, transit 4
$V_{\text{sys}}$ ( $\text{km s}^{-1}$ )	$-2.76 \pm 0.04$	This work
$K_p$ ( $\text{km s}^{-1}$ )	$231 \pm 3$	Yan et al. 2019
$M_p$ ( $M_{\text{Jup}}$ )	$2.16 \pm 0.20$	Yan et al. 2019
$T_{\text{eq}}$ (K)	$2710 \pm 50$	Yan et al. 2019

account for the differences between his results and ours and show how the application of his model to our dataset reproduces our value of  $i_s$  and of the stellar quadrupole moment (see below).

Previous analyses of the precession of WASP-33b by Johnson et al. (2015) and Watanabe et al. (2020) assumed that the stellar spin angular momentum is much larger than the orbital angular momentum because they adopted the gyration radius  $\gamma$  typical of a Sun-like star following the exploratory calculations by Iorio (2011). Here, we determine more appropriate values of the gyration radius and apsidal motion constant  $k_2$  of WASP-33 by making use of the tabulations of Claret (2019). Considering the uncertainties in the stellar mass and effective temperature,

we find that Claret’s model with solar metallicity and mass of  $1.6 M_{\odot}$  is adequate to describe WASP-33. Taking into account the correction for its fast rotation, we find  $\log k_2 = -2.55 \pm 0.014$  and  $\gamma = 0.1884 \pm 0.0019$ , where the uncertainties only take into account the uncertainty in the stellar effective temperature.

With the above values of  $k_2$ ,  $\gamma$ , and the adopted stellar and planetary parameters, we predict a value of  $di/dt = 0.315 \pm 0.026$  (0.0023; 0.0068)  $\text{deg yr}^{-1}$  and a precession rate of the nodes of  $-0.316 \pm 0.026$  (0.0024; 0.0069)  $\text{deg yr}^{-1}$  using the formulae given in Appendix A.3. The coincidence of these numerical values comes from the geometry of the system as explained there. These precession rates differ by less than a half standard deviation from the observed ones, supporting the correctness of the adopted stellar parameters. With our value of  $\gamma$  and the adopted system parameters, we find that the ratio of the stellar spin to the orbital angular momentum is  $2.75 \pm 0.33$ , therefore we cannot neglect the precession of the stellar spin. It occurs within the same period as the precession of the node of the orbital plane and makes the inclination  $i_s$  of the stellar spin axis to the line of sight vary between  $67.5^\circ$  and  $110.8^\circ$  along a complete precession cycle. We note that an inclination of the stellar spin greater than  $90^\circ$  implies that the south pole of the star is in view, so the apparent stellar rotation is clockwise, contrary to the usual anticlockwise rotation assumed when  $i_s < 90^\circ$  and the north pole is in view.

The fast stellar rotation produces a deformation in the stellar mass distribution and hence a distortion in the gravitational field. The stellar gravitational quadrupole moment  $J_2$  can be deduced from the observed nodal precession rate of the orbital plane according to Eq. (3) of Johnson et al. (2015) and is  $(6.73 \pm 0.22$  [0.062; 0.18])  $\times 10^{-5}$ . This value compares well with the theoretically expected value of  $(6.53 \pm 0.41$  [0.011; 0.031])  $\times 10^{-5}$  (e.g. Ragozzine & Wolf 2009, and Appendix A.4), thus confirming the goodness of the adopted values of  $k_2$  and  $\gamma$ . It also supports the hypothesis that WASP-33b is the only close massive planet in the system because another similar body would contribute to the orbital precession rate if its orbit were not coplanar with that of WASP-33b. The fast rotation of WASP-33 makes its quadrupole moment  $\sim 375$  times larger than the solar value ( $J_{2\odot} \sim 1.8 \times 10^{-7}$ ; Rozelot et al. 2009), the effect of the centrifugal force being only modestly compensated by the stronger density concentration in an A-type star.

## 4. Radial velocities

Since we could not exploit the cross-correlation functions (CCFs) from the DRS, RVs were extracted following the method presented in Borsa et al. (2019). Instead of using a Gaussian fit, we preferred to model the LSD lines with a rotational profile (Gray 2008). We measured a  $v \sin i_s = 86.4 \pm 0.5 \text{ km s}^{-1}$ , taken as the average of the out-of-transit measurements and their standard deviation, which is well in agreement with previous values ( $v \sin i_s = 86.63 \text{ km s}^{-1}$ , Johnson et al. 2015). The extracted RVs are listed in Table B.1. We subtracted the difference from the mean of the in-transit RVs from each transit observation to avoid any possible offset caused by instabilities, long-term pulsations, and trends in the orbital solution (e.g. Borsa et al. 2019). We then averaged the RVs of the four transits in bins of 0.005 in phase. The RV time series of each single transit analysed and their average are shown in Fig. 3.

Although stellar pulsations also dominate the RV curve, it is evident a qualitative agreement with the theoretical RM curve calculated using the parameters presented in Table 2 (by using

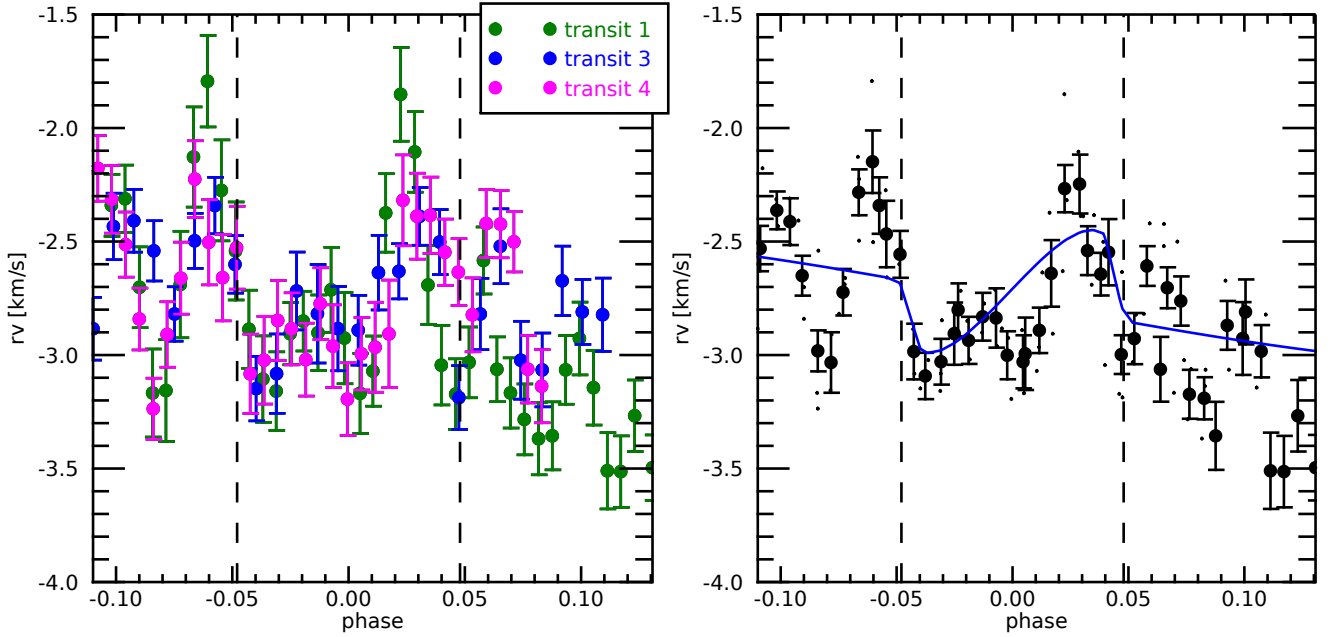


**Fig. 3.** *Left panel:* phase folded RVs of the three analysed HARPS-N transits of WASP-33b. Different colours refer to different transits. *Right panel:* RVs of the three transits averaged in bins of 0.005 in phase (filled circles), together with single RVs (small dots). The blue line represents the theoretical RV solution calculated with the parameters of Table 2 (the values of  $\lambda$  and  $i$  are obtained from the average of the three transits).

the formalism of Ohta et al. 2005). This is further confirmation that for fast rotators the method of fitting the mean line profiles with a rotational profile instead of a Gaussian function brings optimal results, as was previously found for other targets (e.g. Anderson et al. 2018; Johnson et al. 2018; Borsa et al. 2019; Rainer et al. 2021). We note, however, that for this case the Doppler tomography method remains the preferred one to determine the projected spin-orbit inclination angle.

## 5. Balmer lines absorption in the transmission spectrum

We studied the atmosphere of WASP-33b using the technique of transmission spectroscopy, focusing on H $\alpha$  and H $\beta$  absorption, and taking into account the possible contamination given by stellar effects.

### 5.1. Transmission spectrum extraction

We performed transmission spectroscopy following the method of Wyttenbach et al. (2015), applying the following steps independently to each transit. First, we shifted the spectra to the stellar radial velocity rest frame using a Keplerian model of the system. Then we normalised each spectrum by dividing for the average flux within defined wavelength ranges where telluric and stellar lines are not present.

Using the out-of-transit spectra only, we built a telluric reference spectrum  $T(\lambda)$ , by means of a linear correlation between the logarithm of the normalised flux and the air mass (Snellen et al. 2008; Vidal-Madjar et al. 2010; Astudillo-Defru & Rojo 2013), and we then re-scaled all the spectra as if they had been observed at the air mass corresponding to that at the centre of the transit. We then created a master stellar spectrum  $S_{\text{master}}$  by averaging all the out-of-transit spectra (excluding the phase range of the immediate pre-transit, see Sect. 6), and divided all the single spectra for this  $S_{\text{master}}$  creating the residual spectra  $S_{\text{res}}$ .

Every  $S_{\text{res}}$  was then shifted considering the theoretical planetary RV and the systemic velocity of the system, meaning that we placed the spectra in the planetary reference frame. Here, we expect to detect the exoplanetary atmospheric signal centred at the laboratory wavelengths. All the full-in-transit  $S_{\text{res}}$  were then averaged to create the transmission spectrum. At this stage, the transmission spectrum of the planet still includes spurious stellar contaminations.

### 5.2. Removal of CLV + RM

The star over which the planet transits is not a simple homogeneous disc, but it rotates and has a surface brightness that changes as a function of the distance from centre. Effects such as centre-to-limb variations (CLV) and RM have been proven to significantly modify the shape of line profiles, possibly causing false atmospheric detections (e.g. Yan et al. 2017; Borsa & Zannoni 2018; Casasayas-Barris et al. 2020). We thus took these effects into account by creating a model following the methodology described in Yan et al. (2017). The star is modelled as a disc divided into sections of  $0.01 R_s$ . For each point, we calculated the  $\mu$  value (where  $\mu = \cos \theta$ , with  $\theta$  the angle between the normal to the stellar surface and the line of sight) and the projected rotational velocity (by assuming rigid body rotation and re-scaling the  $v \sin i_s$  value of Table 2). A spectrum is then assigned to each point of the grid by quadratically interpolating on  $\mu$  and Doppler-shifting for the stellar rotation the model spectra created using the tool Spectroscopy Made Easy (SME, Piskunov & Valenti 2017), with the line list from the VALD database (Ryabchikova et al. 2015) and the MARCS (Gustafsson et al. 2008) stellar atmospheric models (assuming local thermodynamic equilibrium approximation). The model spectra are created with null rotational velocity for 21 different  $\mu$  values, and adapted to the resolving power of the instrument. Then, using the orbital information from Table 2 we simulate the transit of the planet, calculating the stellar spectrum for different orbital phases as the average spectrum of the non-occulted modelled

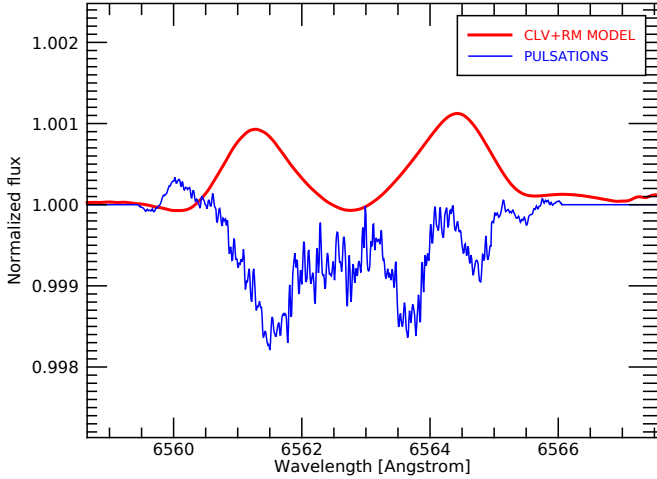


**Fig. 4.** Corrections for CLV +RM and for stellar pulsations applied to the transmission spectrum in the  $H\alpha$  zone.

sections. In the last step, we divide each spectrum for a master stellar spectrum calculated out of transit, obtaining the information of the impact of RM + CLV effects at each in-transit orbital phase. We then move everything in the planetary rest frame and calculate the simulated CLV+RM effects on the transmission spectrum (Fig. 4). We note that we do not take into account the possible deformation of the line profiles given by gravity darkening, which are, however, not expected to be significant (see e.g. Kovács et al. 2013).

### 5.3. Removal of pulsations

Another contamination one has to deal with in this particular case of WASP-33b comes from the stellar pulsations. In Sect. 3, we show how strongly they impact the mean line profiles. In the same way, they have an impact on the extracted planetary transmission spectrum. To deal with this, we opted for an approach similar to that presented in Borsa & Zannoni (2018) to remove the RM from the transmission spectrum using real observing data. This was done by exploiting the S/N of the mean line profiles. We note that pulsations and RM cannot be removed together in this way. This is because the amplitude of the RM effect is dependent on the planetary effective radius in the narrow band passes where the planetary lines are present. On the contrary, the amplitudes of pulsations vary on a much larger wavelength range and can be assumed constant in each of our narrow band passes of interest. In the following, we make the assumption that the pulsation pattern behaves in the same way for all the absorption lines. We use the pulsation pattern extracted from the mean line profile (which is basically based on metal lines) and assume that it is also valid for the Balmer lines, except for a scaling factor. To justify this assumption, we note that the short periods of  $\delta$  Sct are not able to produce significant phase shifts between the photospheric stellar lines of different species and excitation potentials. Moreover, the broadening of the Balmer lines largely affects the wings, but not so much the centre, where we search for the in-transit planetary RVs: Balmer and metallic line profiles are very similar there. We also note that we cannot analyse the pulsation pattern directly on the Balmer lines, due to their low S/N. As a final test, we verified that the applied correction does not impact the depth of the retrieved planetary line profile (Sect. 5.4).

We started from the mean line profiles' residuals after the division for an average out-of-transit mean line profile. We then subtracted the Doppler shadow models calculated in Sect. 3 for each transit (e.g. Fig. 5). Then we created a transmission spectrum of the pulsations ( $TS_{\text{puls}}$ ) in the wavelength region of interest. First, we put together the three transits, then we move from the velocity to the wavelength space, taking the laboratory wavelength of the  $H\alpha$  (Fig. 6) and  $H\beta$  lines as a zero reference, since these are the lines we aim to correct. Then, we moved each mean line-profile residual to the planetary rest frame and averaged the full in-transit residuals to calculate the  $TS_{\text{puls}}$ . At this point, we still have to correct for the magnitude of the effect: the calculated  $TS_{\text{puls}}$  is in fact referred to a line of which the depth is identical to that of the mean line profile and has to be re-scaled to the depth of the line that we want to correct (Borsa & Zannoni 2018). We thus multiplied the amplitude of the correction for a factor which is the ratio between the depth of the mean line profile and that of the  $H\alpha$  (or  $H\beta$ ) line, and we obtained the final spectrum used to correct for pulsations (Fig. 4).

### 5.4. Balmer lines absorption

We corrected the transmission spectrum extracted in Sect. 5.1 from stellar effects by dividing it for the corrective spectra calculated in Sects. 5.2 and 5.3. We note that the effect of pulsations overcome that of CLV +RM by a factor of  $\sim 1.5$  in magnitude (Fig. 4). We find an excess absorption in the  $H\alpha$  region with a contrast of  $0.54 \pm 0.04\%$  and a FWHM of  $36.7 \pm 3.3 \text{ km s}^{-1}$  (Fig. 7). We can translate the contrast into an effective planetary radius  $R_{\text{eff}} = 1.18 \pm 0.02 R_p$ , calculated assuming  $R_{\text{eff}}^2/R_p^2 = (\delta + h)/\delta$ , with  $\delta$  the transit depth (from Table 2) and  $h$  the line contrast (e.g., Chen et al. 2020). As for KELT-9b, the  $H\alpha$  profile of WASP-33b forms in the atmospheric region below the Roche lobe, which can be found at about 1.6 planetary radii. Therefore, this detection does not directly probe atmospheric escape, but it would enable one to set constraints on the planetary temperature-pressure structure and thus on the energetics possibly driving escape. The line has a significant blueshift of  $-8.2 \pm 1.4 \text{ km s}^{-1}$ , indicative of winds in the planetary atmosphere. We note that without the correction for the stellar pulsations, we find a comparable depth (0.53%) but a larger FWHM ( $55 \text{ km s}^{-1}$ ). As they are non-radial pulsations, their averaged effect on the three transits tends to be smaller in the centre of the stellar line profile, and this is also reflected in the transmission spectrum. This is also noticeable in Figs. 4 and 6.

Checking the reference frame of the detections is fundamental when we want to be sure they are caused by the planetary atmosphere and not by spurious stellar effects (e.g. Brogi et al. 2016; Borsa & Zannoni 2018). This is particularly true for this case, where the strong stellar pulsations may not be perfectly corrected for and could mimic atmospheric features. We thus verified that our  $H\alpha$  absorption detection is in the planetary rest frame by resolving it in the 2D tomographic map (Fig. 8), which shows the position of the absorption signal as a function of the orbital phase.

We also find an excess absorption in the  $H\beta$  line region with a contrast of  $0.28 \pm 0.06\%$ , FWHM of  $23.5 \pm 6.3 \text{ km s}^{-1}$  and a blueshift of  $-6.6 \pm 2.6 \text{ km s}^{-1}$  (Figs. 9 and 10). We can translate the contrast into an effective planetary radius  $R_{\text{eff}} = 1.09 \pm 0.03 R_p$ .

We note that the values of absorption depth we obtain are almost half of those obtained for the same planet by Yan et al. (2021) ( $0.99 \pm 0.05\%$  for  $H\alpha$  and  $0.54 \pm 0.07\%$  for  $H\beta$ , respectively). However, the  $H\alpha/H\beta$  line depth ratio is the same

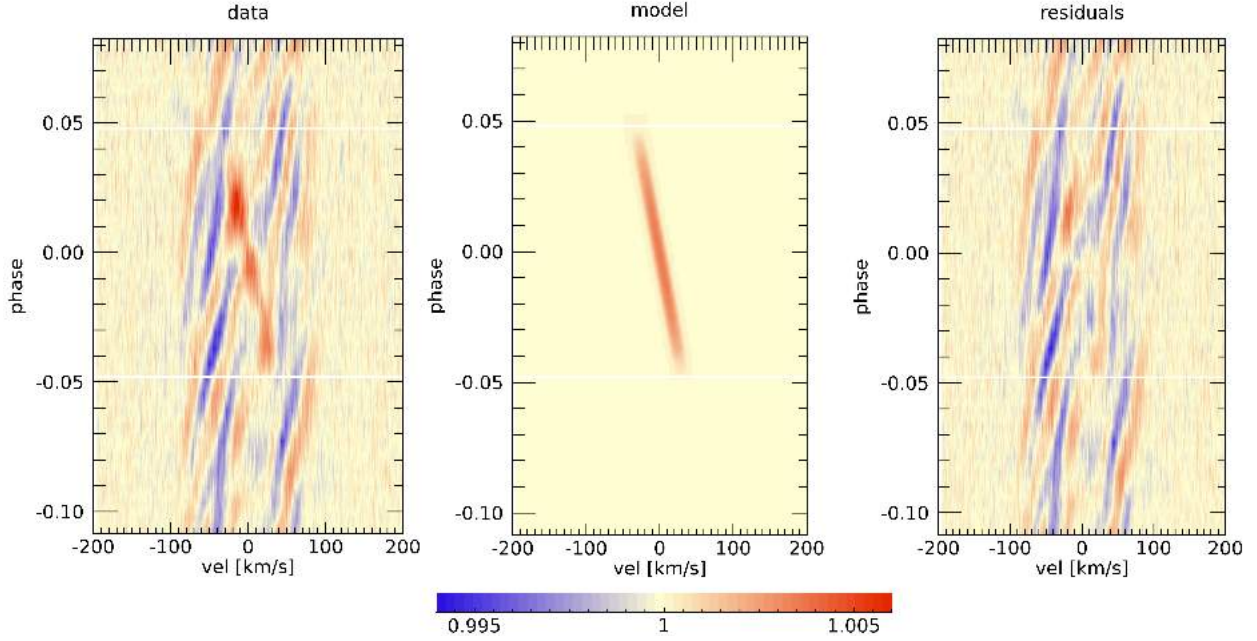


**Fig. 5.** Example of the removal of the Doppler shadow from the mean line profile residuals for transit 4. *Left panel:* original mean line-profile residuals. *Central panel:* model of the Doppler shadow. *Right panel:* mean line profile residuals after the removal of the Doppler shadow. The horizontal white lines show the beginning and end of the transit.

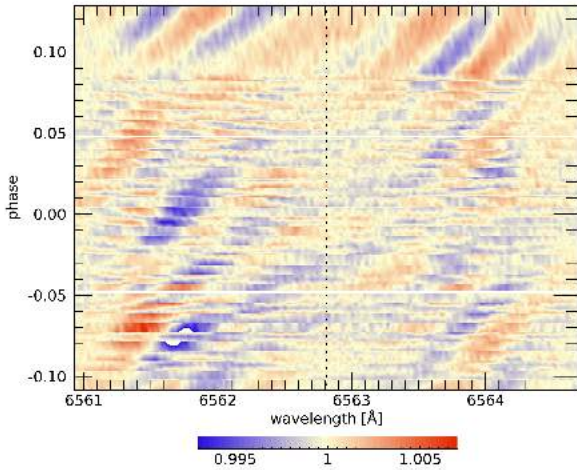


**Fig. 6.** Effect of the pulsation contamination on the three analysed transits as it affects the  $H\alpha$  line, in the stellar rest frame. The vertical dotted line marks the position of the  $H\alpha$  line. The horizontal white lines show the beginning and end of the transit.

( $1.93 \pm 0.44$  for us versus  $1.83 \pm 0.26$  for them). Given the fact that another analysis of these lines also shows different line profile depths ( $1.68 \pm 0.02\%$  for  $H\alpha$  and  $1.02 \pm 0.05\%$  for  $H\beta$ , Cauley et al. 2021), we highlight the possibility that the amplitude of the lines could be variable with time and with the level of the stellar activity (e.g. Borsa et al. 2021) and pulsations. We checked within the dataset we analysed and did not find evidence of significant variability among the three transits with the same  $H\alpha$  contrast.

A future common analysis of all available datasets will help to shed light on the possibility of the observed transit depth variations being related to stellar activity and pulsation, rather than being caused by systematics between different analyses. Furthermore, such an analysis will enable one to obtain a very

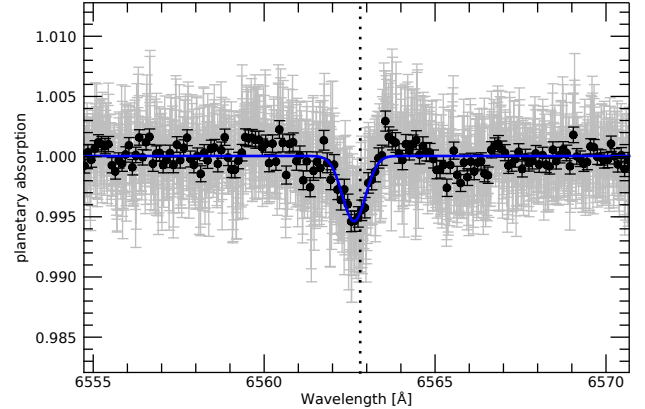


**Fig. 7.**  $H\alpha$  absorption after the correction for stellar effects (RM + CLV and pulsations). Black circles represent  $0.1 \text{ \AA}$  binning. The blue line is the Gaussian best fit. The vertical dotted line shows the planetary  $H\alpha$  rest frame.

high-quality average line profile for each detected Balmer line. These profiles can then be used to constrain the temperature structure of the planetary atmosphere in the  $10^{-3}$ – $10^{-9}$  bar range (e.g. Fossati et al. 2020), going beyond the analysis of Yan et al. (2021), who employed an isothermal profile and assumed local thermodynamical equilibrium. Indeed, it has been shown that, when modelling the Balmer lines detected in the transmission spectrum of the UHJ KELT-9b, these assumptions are invalid (Fossati et al. 2020). Because of similarities in the temperature profile of the upper atmosphere of KELT-9b and WASP-33b (e.g. both present a thermal inversion in the upper atmosphere and reach upper atmospheric temperatures of the order of 10 000 K; Fossati et al. 2018a, 2020), it is likely that the assumptions employed by Yan et al. (2021) to model the Balmer lines led them to obtain unreliable results.

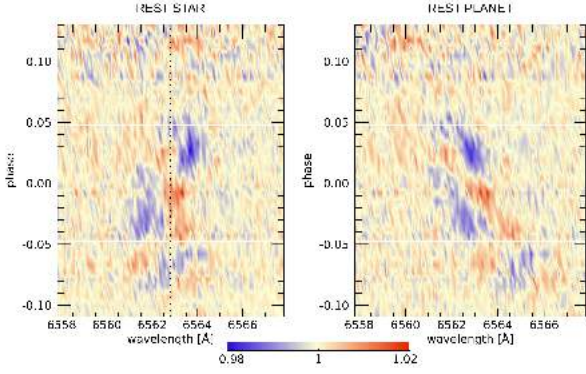


**Fig. 8.** Contour 2D tomography map of  $H\alpha$  absorption in the stellar (*left panel*) and planetary (*right panel*) rest frames, before applying the stellar contamination correction (this also evidences the Doppler shadow, i.e. the red track). The white horizontal lines represent the beginning and end of the transit. The vertical dotted black line shows the  $H\alpha$  planetary rest frame in the right panel and the stellar rest frame in the left panel. A pre-transit signal, not centred in the planetary rest frame, is evident (see discussion in Sect. 6).

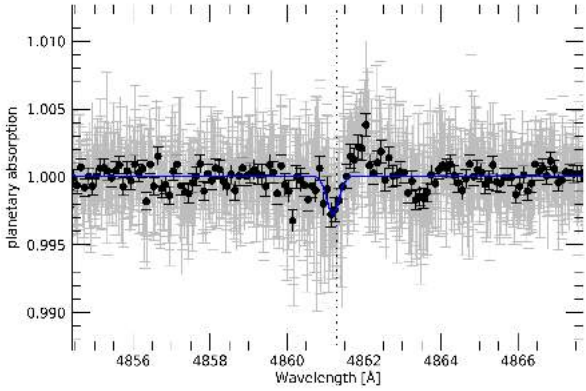


**Fig. 9.** Same as Fig. 7, but for  $H\beta$ .

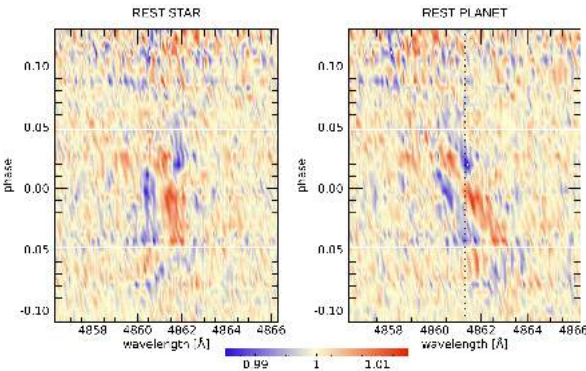


**Fig. 10.** Same as Fig. 8, but for  $H\beta$ .

## 6. Pre-transit signal

Looking at the tomographic map of the  $H\alpha$  absorption (Fig. 8), we note a pre-transit feature. This feature has a different slope and duration in the 2D tomographic map with respect to the dominant pulsation pattern in the mean line profiles (see Figs. 1 and 11). We checked the single transits individually and found that this feature looks quite similar in all four available transits (Fig. 11; see the blue diagonal track before the beginning of the

transit). It is thus something that happens in an almost coherent timing with the orbital period of the planet.

It appears to be a pseudo-absorption pre-transit signal (PTS) happening on the stellar surface, because it moves from  $-v \sin i_s$  to  $+v \sin i_s$  (i.e. across the stellar CCF) with time. We thus investigated this more in detail, performing the normalisation on an extended out-of-transit baseline to avoid including the PTS. By visual inspection, we note that a similar behaviour is observed in many single lines, not only on  $H\alpha$ . On the mean line profiles, it is hidden by the other stellar pulsations, but is still noticeable after removing them (Fig. 1, right panel). Curiously, this feature is also reflected in the radial velocities (see Fig. 3).

By studying it on the  $H\alpha$  line and assuming it is moving with a Keplerian motion around the star with the same orbital period of the planet, we found that the rest frame of the PTS is not compatible with the one of the planet. Thus, we define  $K_{PTS}$  as the Keplerian semi-amplitude of this pseudo-orbital motion. By fitting Gaussian functions and maximising the contrast of their average, we could estimate that the PTS is moving at a  $K_{PTS} \sim 460 \text{ km s}^{-1}$  and is centred at phase  $\sim -0.07$ . As averaged on these values, the PTS has a contrast of  $0.61 \pm 0.06\%$  (Fig. 12). Curiously, the value of the  $K_{PTS}$  is almost double of that of  $K_p$  ( $231 \text{ km s}^{-1}$ , Table 2). The two shoulders around the profile (Fig. 12) and the red tracks around the signal (Fig. 11) mimic the presence of a Doppler shadow, but this could possibly be due to a normalisation artifact (e.g. Snellen et al. 2010). Yan et al. (2021) do not find any signs of pre-transit absorption in their  $H\alpha$  analysis of WASP-33b, but we note that they looked in the planetary rest frame only, while we noticed this PTS while looking in the stellar rest frame.

Many photometric transit observations of WASP-33b have been gathered (see Sect. 1), and even if they are affected by the stellar pulsations, none of them reported a pre-transit reduction of flux coherent with the planetary orbital period. The most probable option in our opinion is that the PTS is still a stellar pulsation mode, which is possibly excited by the planetary companion just before the transit. The PTS likely belongs to the same pulsation pattern that is well visible on  $H\alpha$  and  $H\beta$  lines in Cauley et al. (2021, see their Fig. 5) and also noticeable in the right panel of Fig. 1. When averaging different transits, the PTS does not average out like the other pulsations, but it tends to clearly stand out beyond the noise. This would indeed be evidence of a somewhat expected star-planet interaction for this system. Mechanisms that can excite stellar pulsations could have tidal or magnetic origin.

Planet-induced stellar pulsations were reported for example in the HAT-P-2 system, where de Wit et al. (2017) discovered pulsation modes corresponding to exact harmonics of the planet's orbital frequency, which is indicative of a tidal origin. Planetary-induced tides in the host star, manifesting as the second harmonics of the orbital frequency, were also proposed for the systems WASP-12 and WASP-18 (Maciejewski et al. 2020a,b). Tidally induced flux modulations are also shown in heartbeat stars (e.g. Welsh et al. 2011; Thompson et al. 2012) as a result of large hydrostatic adjustments due to the strong gravitational distortion they experience during the periastron passage of the eccentric binary companion. We thus can hypothesise a tidal star-planet interaction to be the cause of the PTS. When considering equilibrium tides, we should find two RV maxima/minima during the planetary orbit, but the effect should be of the order of  $\sim 10 \text{ m s}^{-1}$  (i.e. lower than the one seen for WASP-18 considering the masses and orbital configuration of the two systems), thus not detectable. When dealing with pulsations excited by tides instead, their amplitude could be much larger, but the lack of a

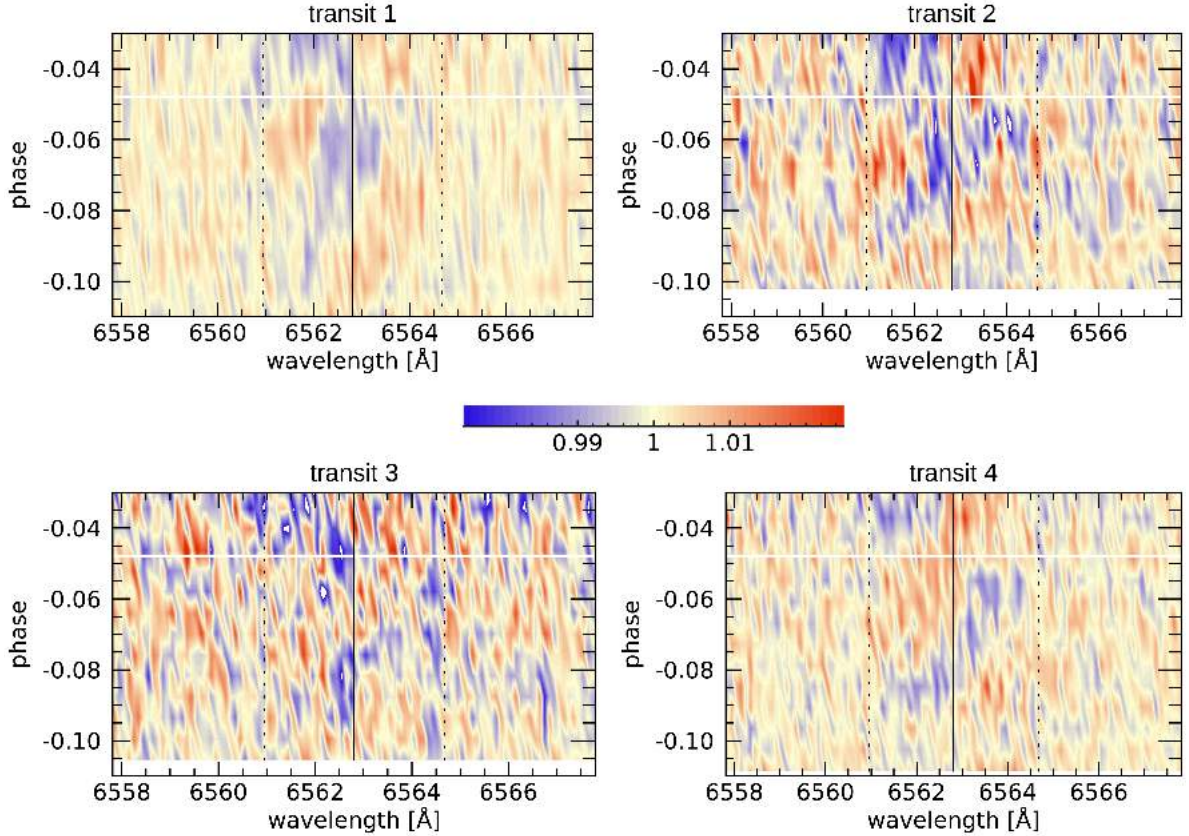


**Fig. 11.** Zoom on the pre-transit signal of the four transits in our dataset, in the stellar rest frame. Vertical line shows the  $H\alpha$  line centre, while vertical dotted lines mark the  $\pm v \sin i_s$  limits. Horizontal white line shows the beginning of the transit. The pre-transit signal is the diagonal blue track before the beginning of the transit.

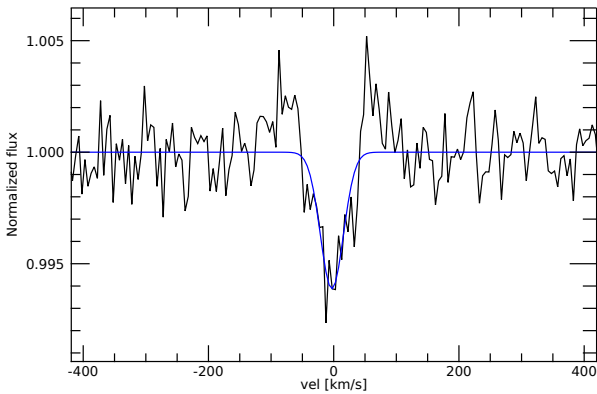


**Fig. 12.** Pre-transit signal profile in its rest frame with  $K_{PTS} = 460 \text{ km s}^{-1}$ . The blue line shows the best-fit Gaussian profile.

stellar pulsation frequency close to the expected period of tides ( $\sim 1.6$  days, assuming a stellar rotational period of 0.884 days and a planetary orbital period of 1.22 days) in the frequencies shown in von Essen et al. (2020) is not in favour of this hypothesis. Moreover, the duration of a resonance between pulsations and tides should be very short with respect to the evolutive timescales of the system. The large oscillations produced by the resonance would in fact dissipate a lot of energy, producing an exchange of angular momentum between rotational and orbital motion that modifies both, quickly moving the system out of the resonance. So, the probability that we are observing the system exactly in this moment is low, which also goes against the tidal hypothesis.

Another possibility for the detected PTS is that of a magnetic interaction. Magnetic star-planet interaction has been proposed and observed for some short-period systems, mainly as the modulation of stellar activity index with the orbital period (e.g. Lanza 2009, 2012; Strugarek 2018; Cauley et al. 2019). A pre-transit absorption in the Balmer lines was observed for HD 189733b (Cauley et al. 2015) and was proposed as being caused by the planetary magnetic field, with a bow shock forming around the magnetosphere moving ahead of the planet (Llama et al. 2013; Cauley et al. 2015). Magnetic fields are known to have an effect on stellar pulsations, depending on their magnitude (e.g. Handler 2013, and references therein). The interesting possibility of the PTS being a magnetic excitation of pulsations given by the interaction with the planetary magnetic field could be further explored with spectro-polarimetric measurements, since magnetic fields affect not only the spectral line profiles but also polarisation properties of stellar radiation (e.g. Landi Degl’Innocenti & Landolfi 2004; Oklopčić et al. 2020).

## 7. Cross-correlation with templates

Since we found the  $K_{PTS}$  to be almost double the planetary  $K_P$  (Sect. 6), we tried to test a possible relation of the PTS with the planetary atmosphere, which could have left aliases, reflections or scattering in the spectra after removing the stellar master. We thus consulted our planetary transmission spectrum for species that could be present only in the planet atmosphere and not in the star. These are to be further investigated in the PTS rest frame in case of detection. We decided to look for Vanadium (V I), which has already been detected in an exoplanetary atmosphere and not

in the host star (Ben-Yami et al. 2020; Borsa et al. 2021), and for aluminum oxide (AlO), which has been claimed to be present in the atmosphere of WASP-33b as a result of low-resolution spectrophotometric observations (von Essen et al. 2019).

Planetary atmosphere transmission models were created using `petitRADTRANS` (pRT, Mollière et al. 2019). We assumed solar abundances, a continuum pressure level of 1 mbar, and an atmospheric temperature-pressure profile calculated for the planet in the same way as presented in Fossati et al. (2020). These parameters were set because they are typical for UHJs (e.g. Hoeijmakers et al. 2019; Stangret et al. 2020). The atmospheric models, created in planetary radius as a function of wavelength, were translated into flux  $(R_p/R_s)^2$ , convolved at the HARPS-N resolving power, and continuum normalised. While for V I we used the opacities already included within pRT, for AlO we used those available at the opacity database of the Exoplanet Simulation Platform<sup>1</sup> (Grimm & Heng 2015), which we arranged in the pRT format.

Cross-correlation between the data and the models was performed in the stellar rest frame on single residual spectra after the removal of a master out-of-transit star and telluric contamination (with the procedures explained in Sect. 5) on the whole wavelength range. This was done by working on the bidimensional  $e2ds$  HARPS-N spectra order by order. We define the cross-correlation as

$$C(v, t) = \sum_{i=1}^N x_i(t, v) T_i, \quad (1)$$

where  $T$  is the model template normalised to unity, and  $x$  are the normalised fluxes at the  $N$  wavelengths  $i$  of the spectra taken at time  $t$  and shifted at velocity  $v$ . In this way, we preserve the flux information (e.g. Hoeijmakers et al. 2019). In our models, we impose all the values with contrasts of less than 5% of the maximum in the wavelength range to be zero.

We selected a step of  $1 \text{ km s}^{-1}$  and a velocity range  $[-300, 300] \text{ km s}^{-1}$ , performing the cross-correlation for each order. We performed a  $5\sigma$  clipping and masked the wavelength ranges most affected by telluric contamination. Then, for each exposure we applied a weighted average between the cross-correlations of the single orders, where the weights applied to each order are the inverse of the standard deviation (i.e. the larger the S/N, the higher the weight) times the depths of the lines in the model template. For a range of  $K_p$  values from 0 to  $300 \text{ km s}^{-1}$  (with steps of  $1 \text{ km s}^{-1}$ ), we averaged the in-transit cross-correlation functions after shifting them in the planetary rest frame. This last step is done by subtracting the planetary radial velocity calculated for each spectrum as  $v_p = K_p \times \sin 2\pi\phi$ , with  $\phi$  the orbital phase. In this way, we created the  $K_p$  versus  $V_{\text{sys}}$  maps, which are used to test the planetary origin of any possible signal. We evaluated the noise by calculating the standard deviation of the  $K_p$  versus  $V_{\text{sys}}$  maps far from where any stellar or planetary signal is expected, and in particular where  $|V| > 90 \text{ km s}^{-1}$ .

We find no evidence supporting the presence in the planetary atmosphere either of V I or AlO, giving (model dependent) upper limits of 97 ppm and 17 ppm at the  $3\sigma$  level, respectively. While for V I we are confident in the accuracy of the line list we used, as it has also already brought a clear detection (Borsa et al. 2021), this is not the case for AlO. We performed an injection of our AlO model in our data using the abundance found in the detection by von Essen et al. (2019), and we were able

to recover it with  $\sim 14\sigma$  significance. Although we did not find evidence of its presence with the available opacities, once an accurate AlO line list is available, verifying the claimed presence of AlO in the planetary atmosphere (von Essen et al. 2019) with high-resolution spectroscopy will be possible using this dataset.

## 8. Summary and conclusions

We provide further evidence that WASP-33 is undergoing nodal precession, finding a precession period of  $1108 \pm 19 \text{ yr}$ , slightly longer than that determined by Johnson et al. (2015). We also found that the stellar spin is perpendicular to the line of sight, and determined the gravitational quadrupole moment of the star  $J_2 = (6.73 \pm 0.22) \times 10^{-5}$ , which is in close agreement with the theoretically predicted value of  $(6.53 \pm 0.41) \times 10^{-5}$  (e.g. Ragozzine & Wolf 2009). By increasing the time coverage of WASP-33b spectroscopic transit observations it will be possible to further constrain the precession period and possibly, with the growing precision of new-generation instruments, to also detect relativistic effects (Iorio 2016). It would be important to look for other exoplanets in which we can detect orbital precession (other than WASP-33b and Kepler-13Ab), to increase the statistics and understand if this phenomenon may also depend on the presence of other companions, on the value of the stellar rotation, or on the orbital obliquity of the system.

We find that stellar pulsations contaminate the extracted transmission spectrum of the planet and propose a method to detrend it, which can also potentially be applied to mitigate stellar activity. The detected  $H\alpha$  absorption in the planetary atmosphere extends up to  $\sim 1.18 R_p$ , while absorption in Ca II H&K was detected with an effective radius of  $\sim 1.56 R_p$  (Yan et al. 2019). This confirms the tendency of Ca II H&K and  $H\alpha$  to exist up to the highest layers of the atmospheres of hot Jupiters. The line contrast of the planetary absorption we measured for both  $H\alpha$  and  $H\beta$  lines is lower than previously found in the literature (Yan et al. 2021; Cauley et al. 2021), while their contrast ratio is the same. This opens the possibility that the atmosphere of WASP-33b could be sensitive to a variable level of activity of the star.

We detect a pre-transit signal almost coherent with the orbital period of the planet. The most likely explanation is that this is a stellar pulsation mode, which is excited by the planetary companion. The nature of this possible star-planet interaction is still doubtful, even if we tend to exclude tidal interactions and are more in favour of possible magnetic interactions. Spectropolarimetric observations of the transit and a complete spectroscopic phase coverage, as well as a detailed analysis of stellar pulsations on the line profiles, could help our understanding of the nature of this pre-transit signal.

*Acknowledgements.* We thank the referee for their useful comments that helped improving the clarity of the manuscript. We acknowledge the support by INAF/Frontiera through the ‘‘Progetti Premiali’’ funding scheme of the Italian Ministry of Education, University, and Research and from PRIN INAF 2019. FB acknowledges financial support from INAF through the ASI-INAF contract 2015-019-R0.

## References

- Akinsanmi, B., Barros, S. C. C., Santos, N. C., et al. 2019, *A&A*, **621**, A117
- Anderson, D. R., Temple, L. Y., Nielsen, L. D., et al. 2018, *MNRAS*, submitted [arXiv:1809.04897]
- Arcangeli, J., Désert, J.-M., Line, M. R., et al. 2018, *ApJ*, **855**, L30
- Astudillo-Defru, N., & Rojo, P. 2013, *A&A*, **557**, A56
- Ben-Yami, M., Madhusudhan, N., Cabot, S. H. C., et al. 2020, *ApJ*, **897**, L5
- Borsa, F., & Zannoni, A. 2018, *A&A*, **617**, A134

<sup>1</sup> <https://dev.opacity.iterativ.ch/>

- Borsa, F., Rainer, M., Bonomo, A. S., et al. 2019, *A&A*, **631**, A34
- Borsa, F., Allart, R., Casasayas-Barris, N., et al. 2021, *A&A*, **645**, A24
- Brogi, M., de Kok, R. J., Albrecht, S., et al. 2016, *ApJ*, **817**, 106
- Casasayas-Barris, N., Palle, E., Yan, F., et al. 2020, *A&A*, **635**, A206
- Cauley, P. W., Redfield, S., Jensen, A. G., et al. 2015, *ApJ*, **810**, 13
- Cauley, P. W., Shkolnik, E. L., Llama, J., et al. 2019, *Nat. Astron.*, **3**, 1128
- Cauley, P. W., Wang, J., Shkolnik, E. L., et al. 2021, *AJ*, **161**, 152
- Chen, G., Casasayas-Barris, N., Pallé, E., et al. 2020, *A&A*, **635**, A171
- Claret, A. 2019, *A&A*, **628**, A29
- Claudi, R., Benatti, S., Carleo, I., et al. 2017, *Eur. Phys. J. Plus*, **132**, 364
- Collier Cameron, A., Bruce, V. A., Miller, G. R. M., et al. 2010a, *MNRAS*, **403**, 151
- Collier Cameron, A., Guenther, E., Smalley, B., et al. 2010b, *MNRAS*, **407**, 507
- Cosentino, R., Lovis, C., Pepe, F., et al. 2012, *Proc. SPIE*, **8446**, 84461V
- Cosentino, R., Lovis, C., Pepe, F., et al. 2014, *Proc. SPIE*, **9147**, 91478C
- Covino, E., Esposito, M., Barbieri, M., et al. 2013, *A&A*, **554**, A28
- Damiani, C., & Lanza, A. F. 2011, *A&A*, **535**, A116
- de Wit, J., Lewis, N. K., Knutson, H. A., et al. 2017, *ApJ*, **836**, L17
- Donati, J.-F., Semel, M., Carter, B. D., Rees, D. E., & Collier Cameron, A. 1997, *MNRAS*, **291**, 658
- Eastman, J. 2017, Astrophysics Source Code Library, [[record ascl:1710.003](#)]
- Eastman, J., Gaudi, B. S., & Agol, E. 2013, *PASP*, **125**, 923
- Eastman, J. D., Rodriguez, J. E., Agol, E., et al. 2019, *PASP*, submitted [[arXiv:1907.09480](#)]
- Fabrycky, D. C., & Winn, J. N. 2009, *ApJ*, **696**, 1230
- Fossati, L., Koskinen, T., Lothringer, J. D., et al. 2018, *ApJ*, **868**, L30
- Fossati, L., Koskinen, T., France, K., et al. 2018, *AJ*, **155**, 113
- Fossati, L., Shulyak, D., Sreejith, A. G., et al. 2020, *A&A*, **643**, A131
- Gallet, F., Bolmont, E., Bouvier, J., et al. 2018, *A&A*, **619**, A80
- Gray, D. F., 2008, *The Observation and Analysis of Stellar Photospheres* (Cambridge, UK: Cambridge University Press)
- Grimm, S. L., & Heng, K. 2015, *ApJ*, **808**, 182
- Gustafsson, B., Edvardsson, B., Eriksson, K., et al. 2008, *A&A*, **486**, 951
- Handler, G. 2013, *Planets, Stars and Stellar Systems. Volume 4: Stellar Structure and Evolution*, 207
- Haynes, K., Mandell, A. M., Madhusudhan, N., et al. 2015, *ApJ*, **806**, 146
- Herman, M. K., de Mooij, E. J. W., Huang, C. X., et al. 2018, *AJ*, **155**, 13
- Herman, M. K., de Mooij, E. J. W., Jayawardhana, R., et al. 2020, *AJ*, **160**, 93
- Herrero, E., Morales, J. C., Ribas, I., et al. 2011, *A&A*, **526**, L10
- Hoeijmakers, H. J., Ehrenreich, D., Kitzmann, D., et al. 2019, *A&A*, **627**, A165
- Iorio, L. 2011, *Ap&SS*, **331**, 485
- Iorio, L. 2016, *MNRAS*, **455**, 207
- Johnson, M. C., Cochran, W. D., Collier Cameron, A., et al. 2015, *ApJ*, **810**, L23
- Johnson, M. C., Rodriguez, J. E., Zhou, G., et al. 2018, *AJ*, **155**, 100
- Kovács, G., Kovács, T., Hartman, J. D., et al. 2013, *A&A*, **553**, A44
- Landi Degl'Innocenti, E., & Landolfi, M. 2004, *Astrophysics and Space Science Library*, **307**, Polarization in Spectral Lines
- Lanza, A. F. 2009, *A&A*, **505**, 339
- Lanza, A. F. 2012, *A&A*, **544**, A23
- Lecante, J., Chabrier, G., Baraffe, I., et al. 2010, *A&A*, **516**, A64
- Lehmann, H., Guenther, E., Sebastian, D., et al. 2015, *A&A*, **578**, L4
- Llama, J., Vidotto, A. A., Jardine, M., et al. 2013, *MNRAS*, **436**, 2179
- Lothringer, J. D., Barman, T., & Koskinen, T. 2018, *ApJ*, **866**, 27
- Maciejewski, G., Niedzielski, A., Villaver, E., et al. 2020a, *ApJ*, **889**, 54
- Maciejewski, G., Knutson, H. A., Howard, A. W., et al. 2020b, *Acta Astron.*, **70**, 1
- McLaughlin, D. B. 1924, *ApJ*, **60**, 22
- Mkrtchian, D. 2015, IAU General Assembly 29, 2255391
- Mollière, P., Wardenier, J. P., van Boekel, R., et al. 2019, *A&A*, **627**, A67
- Nugroho, S. K., Kawahara, H., Masuda, K., et al. 2017, *AJ*, **154**, 221
- Nugroho, S. K., Gibson, N. P., de Mooij, E. J. W., et al. 2020, *ApJ*, **898**, L31
- Ogilvie, G. I. 2014, *ARA&A*, **52**, 171
- Ohta, Y., Taruya, A., & Suto, Y. 2005, *ApJ*, **622**, 1118
- Oklopčić, A., Silva, M., Montero-Camacho, P., et al. 2020, *ApJ*, **890**, 88
- Parmentier, V., Line, M. R., Bean, J. L., et al. 2018, *A&A*, **617**, A110
- Piskunov, N., & Valenti, J. A. 2017, *A&A*, **597**, A16
- Piskunov, N., Kupka, F., Ryabchikova, T. A., Weiss, W. W., & Jeffery, C. S. 1995, *A&AS*, **112**, 525
- Ragozzine, D., & Wolf, A. S. 2009, *ApJ*, **698**, 1778
- Rainer, M., Poretti, E., Mistò, A., et al. 2016, *AJ*, **152**, 207
- Rainer, M., Borsa, F., Pino, L., et al. 2021, *A&A*, **649**, A29
- Rossiter, R. A. 1924, *ApJ*, **60**, 1
- Rozelot, J. P., Damiani, C., & Pireaux, S. 2009, *ApJ*, **703**, 1791
- Ryabchikova, T., Piskunov, N., Kurucz, R. L., et al. 2015, *Phys. Scr.*, **90**, 054005
- Smith, A. M. S., Anderson, D. R., Skillen, I., et al. 2011, *MNRAS*, **416**, 2096
- Snellen, I. A. G., Albrecht, S., de Mooij, E. J. W., & Le Poole, R. S. 2008, *A&A*, **487**, 357
- Snellen, I. A. G., de Kok, R. J., de Mooij, E. J. W., et al. 2010, *Nature*, **465**, 1049
- Stangret, M., Casasayas-Barris, N., Pallé, E., et al. 2020, *A&A*, **638**, A26
- Strugarek, A. 2018, *Handbook of Exoplanets*, 25
- Szabó, G. M., Pál, A., Derekas, A., et al. 2012, *MNRAS*, **421**, L122
- Ter Braak, C. J. F. 2006, *Stat. Comput.*, **16**, 239
- Thompson, S. E., Everett, M., Mullally, F., et al. 2012, *ApJ*, **753**, 86
- Vidal-Madjar, A., Arnold, L., Ehrenreich, D., et al. 2010, *A&A*, **523**, A57
- von Essen, C., Czesla, S., Wolter, U., et al. 2014, *A&A*, **561**, A48
- von Essen, C., Mallonn, M., Albrecht, S., et al. 2015, *A&A*, **584**, A75
- von Essen, C., Mallonn, M., Welbanks, L., et al. 2019, *A&A*, **622**, A71
- von Essen, C., Mallonn, M., Borre, C. C., et al. 2020, *A&A*, **639**, A34
- Watanabe, N., Narita, N., & Johnson, M. C. 2020, *PASJ*, **72**, 19
- Welsh, W. F., Orosz, J. A., Aerts, C., et al. 2011, *ApJS*, **197**, 4
- Wytttenbach, A., Ehrenreich, D., Lovis, C., et al. 2015, *A&A*, **577**, A62
- Yan, F., Pallé, E., Fosbury, R. A. E., et al. 2017, *A&A*, **603**, A73
- Yan, F., Casasayas-Barris, N., Molaverdikhani, K., et al. 2019, *A&A*, **632**, A69
- Yan, F., Wytttenbach, A., Casasayas-Barris, N., et al. 2021, *A&A*, **645**, A22

- 
- 1 INAF – Osservatorio Astronomico di Brera, Via E. Bianchi 46, 23807 Merate (LC), Italy  
e-mail: [francesco.borsa@inaf.it](mailto:francesco.borsa@inaf.it)
  - 2 INAF – Osservatorio Astrofisico di Catania, Via S. Sofia 78, 95123 Catania, Italy
  - 3 Dipartimento di Fisica, Università degli Studi di Milano Bicocca, Piazza dell'Ateneo Nuovo, 1, 20126 Milano, Italy
  - 4 INAF – Osservatorio Astrofisico di Arcetri, Largo E. Fermi 5, 50125 Firenze, Italy
  - 5 Space Research Institute, Austrian Academy of Sciences, Schmiedlstrasse 6, 8042 Graz, Austria
  - 6 Department of Physics, University of Warwick, Coventry CV4 7AL, UK
  - 7 INAF – Osservatorio Astrofisico di Torino, Via Osservatorio 20, 10025, Pino Torinese, Italy
  - 8 Centre for Exoplanets and Habitability, University of Warwick, Gibbet Hill Road, Coventry CV4 7AL, UK
  - 9 INAF-IAPS Istituto di Astrofisica e Planetologia Spaziali, Via del Fosso del Cavaliere 100, 00133, Roma, Italy
  - 10 INAF – Osservatorio Astronomico di Padova, Vicolo dell'Osservatorio 5, 35122, Padova, Italy
  - 11 INAF – Osservatorio Astronomico di Palermo, Piazza del Parlamento, 1, 90134, Palermo, Italy
  - 12 INAF – Osservatorio Astronomico di Trieste, via Tiepolo 11, 34143 Trieste, Italy
  - 13 Thüringer Landessternwarte Tautenburg, Sternwarte 5, 07778, Tautenburg, Germany
  - 14 Department of Physics, University of Rome Tor Vergata, Via della Ricerca Scientifica 1, 00133 Rome, Italy
  - 15 Max Planck Institute for Astronomy, Königstuhl 17, 69117, Heidelberg, Germany
  - 16 Fundación Galileo Galilei - INAF, Rambla José Ana Fernández Pérez 7, 38712 Breña Baja, TF, Spain
  - 17 Instituto de Astrofísica de Canarias (IAC), C/Vía Láctea s/n, 38205 La Laguna, TF, Spain
  - 18 Departamento de Astrofísica, Universidad de La Laguna (ULL), 38206 La Laguna, TF, Spain
  - 19 INAF – Osservatorio Astronomico di Capodimonte, Salita Moiariello 16, 80131, Napoli, Italy
  - 20 INAF – Osservatorio di Cagliari, via della Scienza 5, 09047 Selargius, CA, Italy
  - 21 Dip. di Fisica e Astronomia Galileo Galilei – Università di Padova, Vicolo dell'Osservatorio 2, 35122 Padova, Italy

## Appendix A: Angular momentum geometry and precession in the WASP-33 system

### A.1. Tidal timescales

The tidal timescales of the decay of the obliquity of the WASP-33 system and the exchange of angular momentum between the stellar spin and the orbit can be estimated using the tidal model of Leconte et al. (2010) that we modified to make use of the stellar and planetary modified tidal quality factors,  $Q'_s$  and  $Q'_p$ , respectively. We adopted  $Q'_p = 10^5$ , a typical value for a Jupiter-like planet, and  $Q'_s = 5 \times 10^6$ , which corresponds to a strong tidal coupling as expected in late-type stars, but certainly underestimates the tidal timescales for an A-type star (Ogilvie 2014). Possible resonances between tides and stellar pulsations, which could increase the tidal dissipation inside the star, have been excluded by Kovács et al. (2013).

We find a timescale for the decay of the orbital eccentricity of only 0.2 Myr owing to the strong tidal dissipation enforced by the massive star inside the planet, while the decay of the obliquity and the spin-orbit exchange occur on timescales of  $\sim 300$  Myr and  $\sim 1$  Gyr, respectively, because they depend on the much smaller tidal dissipation inside the star. In conclusion, the precession in WASP-33 can be modelled by assuming that the obliquity and the stellar and orbital angular momenta are of constant magnitude, while the orbit can be assumed to have already been circularised (cf. Damiani & Lanza 2011).

### A.2. Determining the geometry of the system

The obliquity  $\epsilon$  of the system is the angle between the angular momentum of the orbital motion, and the spin of the star and is given by (e.g., Damiani & Lanza 2011; Johnson et al. 2015)

$$\cos \epsilon = \cos i \cos i_s + \sin i \sin i_s \cos \lambda, \quad (\text{A.1})$$

where  $i$  is the inclination of the orbital plane, that is, the angle between the line of sight  $\hat{\mathbf{k}}$  (i.e. the direction from the observer on Earth to the barycentre of the system) and the orbital angular momentum  $\mathbf{l}_{\text{orb}}$ ,  $i_s$  the inclination of the stellar spin axis to the line of sight, and  $\lambda$  is the spin-orbit angle projected onto the plane of the sky, which is measured by fitting the Rossiter-McLaughlin effect or modelling the motion of the Doppler shadow of the planet during its transits. The obliquity  $\epsilon$  can be assumed constant on the timescales characteristic of the precession (cf. Sect. A.1).

The total angular momentum of the system  $\mathbf{L}_{\text{tot}}$  is given by the sum of the stellar spin and the orbital angular momentum and is conserved in the absence of external forces (see Fig. A.1). It can be written as follows:

$$\mathbf{L}_{\text{tot}} = I_s \hat{\boldsymbol{\Omega}}_s + \mathbf{l}_{\text{orb}}, \quad (\text{A.2})$$

where  $I_s = M_s(\gamma R_s)^2$  is the moment of inertia of the star of mass  $M_s$ , equatorial radius  $R_s$ , and gyration radius  $\gamma$ , while  $\boldsymbol{\Omega}_s$  is the stellar spin angular velocity that is related to the spectral line rotational broadening as  $v \sin i_s = \Omega_s R_s \sin i_s$ .

The modulus of the total angular momentum can be found by taking the scalar product of Eq. (A.2) by itself and considering that  $\cos \epsilon = \hat{\boldsymbol{\Omega}}_s \cdot \hat{\mathbf{l}}_{\text{orb}}$ :

$$L_{\text{tot}}^2 = I_s^2 \Omega_s^2 + 2I_s \Omega_s l_{\text{orb}} \cos \epsilon + l_{\text{orb}}^2, \quad (\text{A.3})$$

where the modulus of the orbital angular momentum for a circular orbit is

$$l_{\text{orb}} = mna^2, \quad (\text{A.4})$$

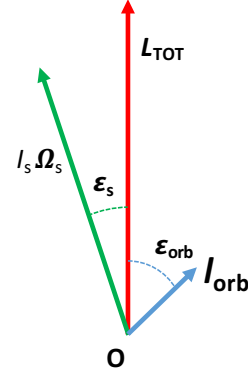


**Fig. A.1.** Total angular momentum of the system  $\mathbf{L}_{\text{tot}}$  (in red) as resulting from the composition of the stellar spin angular momentum  $I_s \boldsymbol{\Omega}_s$  (in green) and the orbital angular momentum  $\mathbf{l}_{\text{orb}}$  (in blue). The angles  $\epsilon_s$  and  $\epsilon_{\text{orb}}$  between the stellar spin or the orbital angular momentum and the total angular momentum, respectively, are indicated. The obliquity of the system is  $\epsilon = \epsilon_s + \epsilon_{\text{orb}}$ , while its projection on the plane of the sky is  $\lambda$  (not indicated).

where  $m = M_s M_p / (M_s + M_p)$  is the reduced mass of the system,  $M_p$  the mass of the planet,  $a$  the semi-major axis of the orbit, and  $n = 2\pi/P_{\text{orb}}$  the orbital mean motion with  $P_{\text{orb}}$  being the orbital period.

Since  $\mathbf{L}_{\text{tot}}$  is constant, taking the scalar product of Eq. (A.2) by the unit vector directed along the line of sight  $\hat{\mathbf{k}}$  and making the derivative with respect to the time gives

$$\frac{di_s}{dt} = -\frac{l_{\text{orb}} \sin i}{I_s \Omega_s \sin i_s} \left( \frac{di}{dt} \right), \quad (\text{A.5})$$

where  $\cos i = \hat{\mathbf{k}} \cdot \hat{\mathbf{l}}_{\text{orb}}$  and  $\cos i_s = \hat{\mathbf{k}} \cdot \hat{\boldsymbol{\Omega}}_s$ .

Taking the time derivative of Eq. (A.1), making use of Eq. (A.5), and considering the system at the particular epoch when  $d\lambda/dt = 0$  and  $di/dt \neq 0$  (as happened in 2011), we obtain an equation that can be solved for  $i_s$ , which is the inclination of the stellar spin to the line of sight:

$$\frac{l_{\text{orb}} \sin i}{I_s \Omega_s \sin i_s} (\sin i \cos i_s \cos \lambda - \cos i \sin i_s) + \sin i \cos i_s - \cos i \sin i_s \cos \lambda = 0. \quad (\text{A.6})$$

The solution of Eq. (A.6) requires a few iterations because  $\Omega_s$  is derived from the spectroscopic  $v \sin i_s$  assuming that the stellar radius  $R_s$  is known. The numerical solution converges very rapidly and we adopt the solution closer to  $\pi/2$  in our model. In principle, the method can be extended to any epoch when  $d\lambda/dt$  and  $di/dt$  can both be measured, but the advantage of considering an epoch when  $d\lambda/dt = 0$  is that of reducing the errors because the equations simplify and only  $di/dt \neq 0$  is required.

To derive the other angles that specify the geometry of the system, we adopted a Cartesian orthogonal reference frame ( $Oxyz$ ) with the origin  $O$  at the barycentre of the system, the polar axis  $\hat{\mathbf{z}}$  directed along the total angular momentum, and the  $\hat{\mathbf{x}}$  axis in the plane defined by the vectors  $\mathbf{L}_{\text{tot}}$  and the line of sight (cf. Fig. A.2).

We introduce the angle  $\beta$  between the total angular momentum  $\mathbf{L}_{\text{tot}}$  and the unit vector  $\hat{\mathbf{s}}$  directed opposite the line of sight, meaning from the barycentre of the system towards the observer, namely  $\hat{\mathbf{s}} \equiv -\hat{\mathbf{k}}$  and  $\cos \beta = \hat{\mathbf{L}}_{\text{tot}} \cdot \hat{\mathbf{s}}$ . We also introduced the angles  $\epsilon_s$  and  $\epsilon_{\text{orb}}$  between the total angular momentum and the stellar spin and orbital angular momentum, respectively; that is,

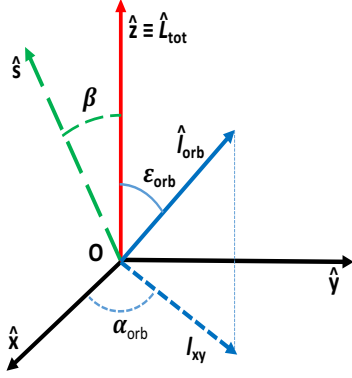


**Fig. A.2.** Reference frame adopted to specify the geometry of the WASP-33 system. The origin  $O$  is at the barycentre of the system; the  $\hat{z}$  axis is directed along the total angular momentum of the system (in red); and the  $\hat{x}$  axis is in the plane defined by the line of sight and the total angular momentum. The vector  $\hat{s}$  (dashed in green) is directed opposite the line of sight, meaning from the barycentre of the system towards the observer on Earth. The unit vector in the direction of the orbital angular momentum  $\hat{l}_{\text{orb}}$  is depicted in blue (solid line), together with its projection  $I_{xy}$  on the  $xy$  plane (dashed line), and the angle  $\alpha_{\text{orb}}$  between that projection and the  $\hat{x}$  axis. The angle  $\alpha_{\text{orb}}$  varies uniformly in our inertial reference frame due to the precession of the orbital plane (see the text). For simplicity, the stellar spin vector and its projection on the  $xy$  plane are not shown.

$\cos \epsilon_s = \hat{\mathbf{L}}_{\text{tot}} \cdot \hat{\boldsymbol{\Omega}}_s$  and  $\cos \epsilon_{\text{orb}} = \hat{\mathbf{L}}_{\text{tot}} \cdot \hat{\mathbf{l}}_{\text{orb}}$  (see Fig. A.1). In our reference frame,

$$\hat{\mathbf{s}} = (\sin \beta, 0, \cos \beta). \quad (\text{A.7})$$

Considering Eq. (A.2) and Fig. A.1, we find the following:

$$\cos \beta = (\hat{\mathbf{s}} \cdot \hat{\mathbf{L}}_{\text{tot}}) / L_{\text{tot}} = -(I_s \Omega_s \cos i_s + l_{\text{orb}} \cos i) / L_{\text{tot}}, \quad (\text{A.8})$$

$$\cos \epsilon_s = (\hat{\mathbf{L}}_{\text{tot}} \cdot \hat{\boldsymbol{\Omega}}_s) / (L_{\text{tot}} \Omega_s) = (I_s \Omega_s + l_{\text{orb}} \cos \epsilon) / L_{\text{tot}}, \quad (\text{A.9})$$

$$\cos \epsilon_{\text{orb}} = (\hat{\mathbf{L}}_{\text{tot}} \cdot \hat{\mathbf{l}}_{\text{orb}}) / (L_{\text{tot}} l_{\text{orb}}) = (I_s \Omega_s \cos \epsilon + l_{\text{orb}}) / L_{\text{tot}}. \quad (\text{A.10})$$

Eqs. (A.8), (A.9), and (A.10) can be used to find the angles  $\beta$ ,  $\epsilon_s$ , and  $\epsilon_{\text{orb}}$ , given that  $\epsilon$  and  $i_s$  have been derived from Eqs. (A.1) and (A.6),  $L_{\text{tot}}$  comes from Eq. (A.3), and the inclination  $i$  of the orbital plane is known from the model of the planetary transits.

To complete the description of the system, we need to derive the nodal angles  $\alpha_s$  and  $\alpha_{\text{orb}}$  between the  $xz$  plane, defined by the vectors  $\hat{\mathbf{L}}_{\text{tot}}$  and  $\hat{\mathbf{s}}$ , and the spin and the orbital angular momentum, respectively. Since the stellar spin and the orbital angular momentum lie in the same plane containing  $\hat{\mathbf{L}}_{\text{tot}}$ ,  $\alpha_s = \pi - \alpha_{\text{orb}}$ , so it is sufficient to derive the latter angle. The components of the unit vector directed along  $\hat{\mathbf{l}}_{\text{orb}}$  can be expressed as (cf. Fig. A.2)

$$\hat{\mathbf{l}}_{\text{orb}} = (\sin \epsilon_{\text{orb}} \cos \alpha_{\text{orb}}, \sin \epsilon_{\text{orb}} \sin \alpha_{\text{orb}}, \cos \epsilon_{\text{orb}}). \quad (\text{A.11})$$

Considering the definition of the cross product, we obtain

$$(\hat{\mathbf{l}}_{\text{orb}} \times \hat{\mathbf{s}})^2 = \sin^2 i. \quad (\text{A.12})$$

By expanding the l.h.s. of Eq. (A.12) by means of Eqs. (A.7) and (A.11), we obtain an equation for  $\alpha_{\text{orb}}$ :

$$A \cos^2 \alpha_{\text{orb}} + B \cos \alpha_{\text{orb}} + C = 0, \quad (\text{A.13})$$

**Table A.1.** The angles and the factor  $H(i, \beta, \epsilon, \alpha_{\text{orb}})$  defining the geometry and the rate of nodal precession of the WASP-33 system at the epoch 19 October 2011 when  $d\lambda/dt = 0$  is assumed. In addition to the standard deviations giving the statistical errors of the parameters, their systematic deviations obtained by shifting the epoch of  $d\lambda/dt = 0$  by 500 days after and before 19 October 2011 are listed, respectively.

	Value [degrees]	Stand. dev. [degrees]	System. dev. [degrees]
$i$	87.56	0.04	
$\lambda$	-114.01	0.22	
$\epsilon$	113.99	0.22	(-0.236; -0.669)
$\epsilon_{\text{orb}}$	92.37	2.73	(-0.239; -0.677)
$\epsilon_s$	21.63	2.72	(0.003; 0.008)
$i_s$	90.11	0.12	(-0.026; -0.015)
$\beta$	90.84	0.17	(-0.135; 0.206)
$\alpha_{\text{orb}}$	92.47	0.06	(-0.414; 0.477)
$\alpha_s$	87.53	0.06	(0.414; -0.477)
$H(i, \beta, \epsilon, \alpha_{\text{orb}})$	-1.0021	0.0024	$(2.1; 3.5) \times 10^{-4}$

where

$$A = \sin^2 \epsilon_{\text{orb}} \sin^2 \beta, \quad (\text{A.14})$$

$$B = \frac{1}{2} \sin(2\beta) \sin(2\epsilon_{\text{orb}}), \quad (\text{A.15})$$

$$C = \sin^2 i - \cos^2 \beta \sin^2 \epsilon_{\text{orb}} - \sin^2 \beta. \quad (\text{A.16})$$

Between the two solutions of Eq. (A.13), we chose the one giving the correct sign of

$$\cos i = -\hat{\mathbf{s}} \cdot \hat{\mathbf{l}}_{\text{orb}} = -\sin \beta \sin \epsilon_{\text{orb}} \cos \alpha_{\text{orb}} - \cos \beta \cos \epsilon_{\text{orb}}. \quad (\text{A.17})$$

The values of the angles specifying the geometry of the WASP-33 system are listed in Table A.1 together with their standard deviations. These are obtained by propagating the standard deviations of the system parameters and the systematic deviations obtained by shifting the epoch when  $d\lambda/dt = 0$  by 500 days after and before the assumed epoch, respectively.

### A.3. Precession of the orbital plane and the stellar spin

The precession of the orbital plane is described by the precession of the vector  $\hat{\mathbf{l}}_{\text{orb}}$  around the total angular momentum  $\hat{\mathbf{L}}_{\text{tot}}$ . In our reference frame, this precession corresponds to a uniform increase (or decrease) of the nodal angle  $\alpha_{\text{orb}}$  as a function of the time. We can compute the precession rate by differentiating Eq. (A.17) with respect to the time, yielding

$$\frac{d\alpha_{\text{orb}}}{dt} = H(i, \beta, \epsilon, \alpha_{\text{orb}}) \left( \frac{di}{dt} \right), \quad (\text{A.18})$$

where

$$H(i, \beta, \epsilon, \alpha_{\text{orb}}) \equiv -\frac{\sin i}{\sin \beta \sin \epsilon_{\text{orb}} \sin \alpha_{\text{orb}}}. \quad (\text{A.19})$$

The factor  $H(i, \beta, \epsilon, \alpha_{\text{orb}})$  is very close to  $-1$  in our system (cf. Table A.1), therefore the rate of nodal precession is virtually identical in absolute value to  $di/dt$ . The minimum and maximum values of the inclination of the orbital plane  $i$ , reached along a complete precession cycle, can be obtained from Eq. (A.17) for  $\alpha_{\text{orb}} = 0, \pi$  and are  $\pi - (\beta \pm \epsilon_{\text{orb}})$ .

Eq. (A.18) can be applied with the observed value of  $di/dt$  to provide the observed rate of precession of the nodes of the planetary orbit; the precession period follows as  $2\pi/(d\alpha_{\text{orb}}/dt)$ . Alternatively, it can be used with the theoretically derived  $di/dt$  to predict the expected nodal precession rate in our system. Specifically, the theoretical expression of  $di/dt$  for a circular orbit according to Eqs. (7) and (11) of Damiani & Lanza (2011) is

$$\frac{di}{dt} = \mathcal{A}_s \Omega^2 \cos \epsilon \sin i_s \sin \lambda, \quad (\text{A.20})$$

where

$$\mathcal{A}_s \equiv \left(\frac{k_2}{n}\right) \left(1 + \frac{M_p}{M_s}\right) \left(\frac{R_s}{a}\right)^5, \quad (\text{A.21})$$

and where  $k_2$  is the apsidal motion constant of the star that depends on its internal density stratification (e.g. Claret 2019). We note that the sign of  $\lambda$  as defined by Damiani & Lanza (2011) is opposite that adopted by Johnson et al. (2015) and by the present analysis; Eq. (A.20) has been reformulated according to the latter convention.

The precession of the stellar spin occurs at the same rate as that of the orbital plane, but in the opposite direction, as can be deduced from the conservation of the total angular momentum. The minimum and maximum inclinations of the stellar spin to the line of sight along a precession cycle can be derived as in the case of the orbital plane and are  $\pi - (\beta \pm \epsilon_s)$ .

#### A.4. Gravitational quadrupole moment of the star

The precession rate can be related to the stellar gravitational quadrupole moment  $J_2$  by means of Eq. (3) of Johnson et al. (2015), which we recast in our notation as

$$J_2 = -\frac{1}{3\pi} \frac{P_{\text{orb}}}{\cos \epsilon} \left(\frac{a}{R_s}\right)^2 \left(\frac{d\alpha_{\text{orb}}}{dt}\right). \quad (\text{A.22})$$

We note that our definition of the longitude of the ascending node of the orbit is different from that adopted by Johnson et al., but the precession rate is the same, independently of the definition, because the precession period is unique for the system.

The gravitational quadrupole moment as derived from the observation of the precession of the orbital plane can be compared with the expectation from the theory. Specifically,  $J_2$  can be described as the sum of the two components,  $J_{2\text{rot}}$  and  $J_{2\text{tide}}$ , which are produced by the centrifugal and the tidal distortion of the star, respectively. Their expressions are as follows (e.g. Ragozzine & Wolf 2009):

$$J_2 = J_{2\text{rot}} + J_{2\text{tide}}, \quad (\text{A.23})$$

$$J_{2\text{rot}} = \frac{2k_2}{3} \left(\frac{\Omega_s^2 R_s^3}{GM_s}\right), \quad (\text{A.24})$$

$$J_{2\text{tide}} = k_2 \left(\frac{M_p}{M_s}\right) \left(\frac{R_s}{a}\right)^3, \quad (\text{A.25})$$

where  $G$  is the gravitation constant. In the case of WASP-33,  $J_{2\text{tide}} \sim 10^{-3} J_{2\text{rot}}$ , therefore it can be neglected in our analysis. More precisely, Eq. (A.25) is valid when the planet is on the equatorial plane of the star, but, given the small size of  $J_{2\text{tide}}$ , this conclusion is not affected.

**Table A.2.** Angles  $\Omega$  and  $I$  of the precession model of Iorio (2016) at the epochs of our transit observations.

Day	Month	Year	$\Omega$ [degrees]	$I$ [degrees]
12	11	2008	$274.00 \pm 0.078$	$111.23 \pm 0.48$
19	10	2011	$272.67 \pm 0.041$	$113.99 \pm 0.22$
4	10	2014	$271.44 \pm 0.039$	$112.90 \pm 0.24$
28	9	2016	$271.11 \pm 0.043$	$111.59 \pm 0.26$
12	1	2018	$270.65 \pm 0.059$	$111.69 \pm 0.40$
2	1	2019	$270.12 \pm 0.039$	$110.83 \pm 0.30$

Finally, we note that we considered the planetary spin synchronised and perpendicular to the orbital plane because tides can enforce such a configuration on a timescale as short as  $\sim 1$  Myr (Leconte et al. 2010). However, if this were not the case, we would have to include the contribution of the planetary gravitational quadrupole moment to the precession of the orbit as discussed by, for example, Ragozzine & Wolf (2009) and Damiani & Lanza (2011). The General Relativity precession is negligible in our case, as it is  $\sim 500$  times smaller than the nodal precession induced by the oblateness of the star (Iorio 2011).

#### A.5. A comparison with the model of Iorio (2016)

Another model of the precession in WASP-33 was presented by Iorio (2016). It assumes a Cartesian reference frame with the  $y$  axis directed towards the observer, the  $z$  axis along the projection of the stellar spin on the plane of the sky, and the  $x$  axis perpendicular to both the other axes to form a right-handed orthogonal coordinate system (see Fig. 1 of Iorio 2016). In such a reference frame, the precession is described through the variation of the angles  $\Omega$ , the longitude of the ascending node of the orbit measured from the  $x$  axis in the  $x-y$  plane, and  $I$ , which is the angle between the  $z$  axis and the orbital angular momentum. We note that the  $x-y$  plane does not coincide with the plane of the sky, while the  $x-z$  plane does coincide with it.

The two angles,  $\Omega$  and  $I$ , can be expressed in terms of the inclination  $i$  of the orbital plane to the plane of the sky and of the projected obliquity  $\lambda$  on the plane of the sky following Eqs. (25) to (33) of Iorio (2016) as follows:

$$\Omega = \arccos \hat{N}_x \text{ for } \hat{N}_y \geq 0, \text{ or} \quad (\text{A.26})$$

$$\Omega = 2\pi - \arccos \hat{N}_x \text{ for } \hat{N}_y < 0, \quad (\text{A.27})$$

where

$$\hat{N}_x = -\frac{\cos i}{\sqrt{\cos^2 i + \sin^2 i \sin^2 \lambda}}, \quad (\text{A.28})$$

$$\hat{N}_y = \frac{\sin i \sin \lambda}{\sqrt{\cos^2 i + \sin^2 i \sin^2 \lambda}}, \quad (\text{A.29})$$

while

$$I = \arccos(\sin i \cos \lambda). \quad (\text{A.30})$$

Using the values of  $i$  and  $\lambda$  listed by Watanabe et al. (2020) and those derived in the present work, we calculated angles  $\Omega$  and  $I$

and listed them in Table A.2 together with their standard deviations obtained by propagating the errors on the inclination and the projected obliquity. The only two observations available to Iorio (2016) were those of 2008 and 2014 with the parameters  $i$  and  $\lambda$  as reported by Johnson et al. (2015), while we adopted the more precise determination of Watanabe et al. (2020). Therefore, Iorio estimated the rate of precession assuming a constant rate of change for both  $\Omega$  and  $I$  between the two epochs that led to an inclination of the stellar spin axis to the line of sight and a stellar quadrupole moment of, in our notation,  $i_s = 142^\circ \pm 11^\circ$  and  $J_2 = (2.1 \pm 0.8) \times 10^{-4}$ , respectively. Nevertheless, as can be seen in Fig. A.3, the situation was different: the angle  $I$  reached a maximum around 2011 and the precession rate  $dI/dt$  became zero at that epoch. By differentiating Eq. (A.30), we see that  $dI/dt$  is zero close to the epoch when  $d\lambda/dt = 0$ , provided that  $i$  is close to  $90^\circ$ , as it is in the case of a transiting planet, although the two epochs only coincide if  $i = 90^\circ$ .

Considering Eq. (9) of Iorio (2016) and that his unit vector  $\mathbf{S}^* = (0, \cos i_s, \sin i_s)$  in our notation, for a circular orbit we have (cf. Section A.1):

$$\frac{dI}{dt} = -\frac{3nJ_2R_s^2}{2a^2} \cos i_s \sin \Omega (\sin i_s \cos I - \cos i_s \cos \Omega \sin I), \quad (\text{A.31})$$

where the symbols have been introduced above. For the given values of the angles  $\Omega$  and  $I$ , Eq. (A.31) implies that  $dI/dt = 0$  when  $\cos i_s = 0$ , which confirms our result that the stellar spin is perpendicular to the line of sight around 2011.

The precession rate of the angle  $\Omega$  at the epoch when  $dI/dt = 0$  is given by Eq. (10) of Iorio (2016), that is,

$$\frac{d\Omega}{dt} = \frac{3nJ_2R_s^2}{2a^2} \cos I \quad (\text{A.32})$$

for a circular orbit. Considering our value of  $J_2 = (6.73 \pm 0.22) \times 10^{-5}$ , we obtain a precession rate  $d\Omega/dt = 0.325 \pm 0.015$  deg/yr in 2011 that is comparable with the observed mean precession rate  $0.353 \pm 0.007$  deg/yr obtained by a linear regression over the six epochs in Table A.2. We do not expect a closer agreement because the precession rate  $d\Omega/dt$  is not constant and the angle  $I$  is also variable and affected by relatively large errors. Therefore, we prefer to estimate  $J_2$  using Eq. (3) of Johnson et al. (2015), because in that formula the precession rate and the true obliquity  $\psi$  are constant, thus allowing a more precise determination.

In conclusion, the differences between the results of Iorio (2016) and ours, as well as those of Watanabe et al. (2020), are due to the paucity of observations available at that time leading to the assumption of constant precession rates for the angles  $\Omega$  and  $I$ . Our more extended dataset allows us to show that the precession rate  $dI/dt$  vanished around 2011, thus reconciling our results with those of Iorio's study and confirming that the inclination of the stellar spin axis to the line of sight was very close to  $90^\circ$  at that epoch.

## Appendix B: Radial velocity table

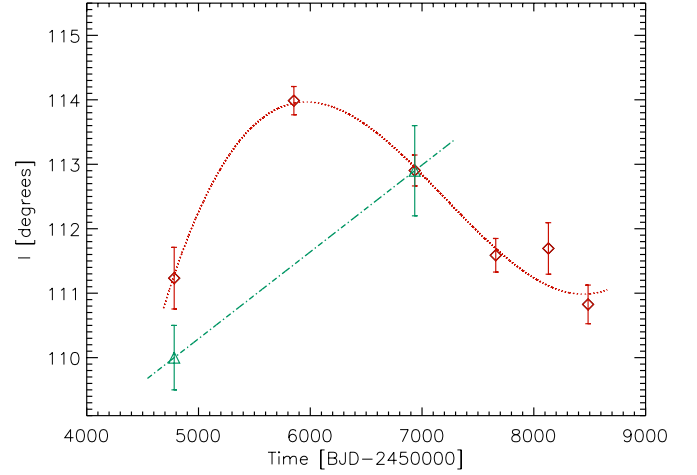


**Fig. A.3.** Angle  $I$  of the model by Iorio (2016) versus the time. The red diamonds are the values found from our dataset, while the green triangles are the two values derived by Iorio from the data available to him at the time of his work. We see that the precession rate  $dI/dt$  is not constant as shown by the cubic interpolation plotted as a dotted red line. For the sake of comparison, we plot a linear interpolation between the two values available to Iorio assuming a constant precession rate.

**Table B.1.** HARPS-N RV observations of WASP-33.

Time [BJD-2450000]	RV [km s <sup>-1</sup> ]	RV error [km s <sup>-1</sup> ]
7660.46966	-2.210	0.137
7660.47683	-2.181	0.148
7660.48443	-2.571	0.178
7660.49131	-3.037	0.194
7660.49830	-3.026	0.224
7660.50580	-2.559	0.235
7660.51275	-1.997	0.221
7660.52008	-1.663	0.202
7660.52736	-2.144	0.222
7660.53481	-2.411	0.216
7660.54183	-2.756	0.172
7660.54914	-2.976	0.190
7660.55612	-3.029	0.173
7660.56343	-2.776	0.137
7660.57031	-2.720	0.132
7660.57806	-2.771	0.166
7660.58493	-2.583	0.187
7660.59189	-2.795	0.201
7660.60012	-3.039	0.176
7660.60686	-2.941	0.155
7660.61359	-2.244	0.173
7660.62139	-1.721	0.207
7660.62879	-1.975	0.177
7660.63575	-2.561	0.174
7660.64275	-2.914	0.175
7660.65028	-3.042	0.155
7660.65731	-2.902	0.156
7660.66485	-2.453	0.148
7660.67192	-2.933	0.143
7660.67904	-3.037	0.155
7660.68626	-3.153	0.156
7660.69377	-3.239	0.159
7660.70097	-3.226	0.150
7660.70797	-2.935	0.151
7660.71520	-2.797	0.160
7660.72256	-3.014	0.165
7660.72983	-3.380	0.168
7660.73690	-3.383	0.157
7660.74419	-3.137	0.158
7660.75355	-3.366	0.144
7682.42344	-2.566	0.111
7682.43060	-2.601	0.118
7682.43791	-2.730	0.129
7682.44515	-2.654	0.121
7682.45238	-2.555	0.122
7682.45945	-2.452	0.144
7682.46686	-2.718	0.164
7682.47396	-3.006	0.152
7682.48140	-2.915	0.160
7682.48844	-2.824	0.153
7682.49562	-2.810	0.147
7682.50304	-3.085	0.148
7682.51000	-2.913	0.170
7682.51738	-2.999	0.163
7682.52458	-2.988	0.177
7682.53171	-2.984	0.171
7682.53903	-2.963	0.167
7682.54636	-2.586	0.185
7682.55371	-2.800	0.220
7682.56072	-2.767	0.217
7682.56810	-2.708	0.208
7682.57520	-2.648	0.188
7682.58247	-2.614	0.199
7682.58974	-2.734	0.183
7682.59696	-2.590	0.164
7682.60426	-2.050	0.166

Table B.1. continued.

Time [BJD-2450000]	RV [ $\text{km s}^{-1}$ ]	RV error [ $\text{km s}^{-1}$ ]
7682.66575	-3.309	0.191
7682.67303	-3.563	0.170
7682.68015	-3.158	0.159
7682.68730	-2.720	0.143
7682.69454	-2.764	0.128
7682.70348	-3.067	0.120
8131.32988	-2.929	0.138
8131.34056	-2.478	0.146
8131.35129	-2.453	0.138
8131.36176	-2.586	0.133
8131.37263	-2.864	0.120
8131.38317	-2.542	0.121
8131.39379	-2.386	0.124
8131.40434	-2.645	0.127
8131.41542	-3.192	0.142
8131.42616	-3.127	0.175
8131.43664	-2.762	0.171
8131.44760	-2.863	0.217
8131.45835	-2.928	0.186
8131.46897	-2.935	0.154
8131.47960	-2.682	0.164
8131.49031	-2.676	0.122
8131.50115	-2.434	0.127
8131.51169	-2.547	0.143
8131.52180	-3.232	0.140
8131.53303	-2.864	0.157
8131.54352	-2.565	0.165
8131.55425	-3.067	0.172
8131.56549	-3.110	0.163
8131.57598	-2.718	0.153
8131.58653	-2.855	0.143
8131.59718	-2.867	0.161
8486.31455	-2.277	0.144
8486.32180	-2.414	0.149
8486.32912	-2.613	0.143
8486.33632	-2.941	0.136
8486.34363	-3.336	0.135
8486.35089	-3.009	0.144
8486.35806	-2.761	0.159
8486.36541	-2.325	0.169
8486.37276	-2.603	0.188
8486.38002	-2.759	0.190
8486.38734	-2.627	0.183
8486.39448	-3.182	0.175
8486.40179	-3.122	0.193
8486.40892	-2.947	0.176
8486.41611	-2.984	0.159
8486.42364	-3.120	0.161
8486.43120	-2.873	0.158
8486.43789	-3.060	0.182
8486.44549	-3.294	0.160
8486.45276	-3.094	0.160
8486.46002	-3.065	0.198
8486.46729	-3.006	0.237
8486.47462	-2.418	0.200
8486.48194	-2.488	0.189
8486.48896	-2.484	0.168
8486.49661	-2.647	0.146
8486.50368	-2.734	0.147
8486.51103	-2.922	0.163
8486.51828	-2.520	0.150
8486.52578	-2.523	0.149
8486.53282	-2.601	0.133
8486.54008	-3.162	0.149
8486.54735	-3.237	0.161